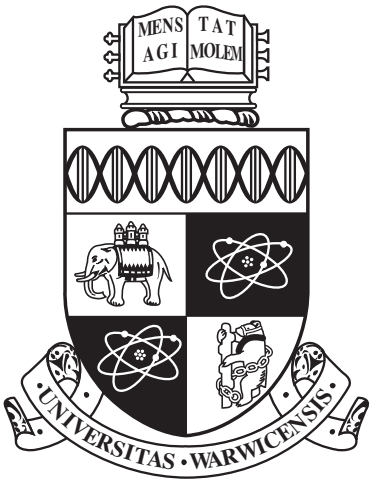

Real-Space Renormalisation Group Approach to Extensions of the Chalker-Coddington Model

by

Syl Shaw

Thesis

Submitted to the University of Warwick

for the degree of

Master of Science by Research

Department of Physics

November 2023

THE UNIVERSITY OF
WARWICK

Contents

List of Tables

List of Figures

Acknowledgments

This project would not exist if not for the constant stream of helpful direction and input from Prof. Rudolf A. Römer, who I want to thank for an exciting and compelling introduction to research in physics. His guidance has been invaluable in my journey towards the completion of this thesis and I am grateful for the opportunities presented to me throughout my time under his supervision. I would also like to thank my family for supporting me in my ambitions, particularly my parents, who only ever encouraged and fostered my passion for learning.

Audrey, Crow, Jack, Nina and everyone else, I could not have done any of this without you. Thank you for being my support every single day, through everything. Thank you for withstanding the weekly (if not daily) incoherent babbling over incomprehensible minutia and trivialities to do with this thesis. Thank you especially for your help throughout the writing period, which has allowed me to push myself to create work that I am proud of.

Declarations

I declare that all work presented in this thesis is truly my own, unless otherwise acknowledged. The work in this thesis does not contribute to the award of any other accreditation in my name, at any other institution.

Abstract

After more than 40 years since its discovery, the quantum Hall effect remains a cornerstone of modern condensed matter physics. The Chalker-Coddington network model depicts the phase transition between quantum Hall plateaux. The model has been utilised to great success in accurately predicting the macroscopic phenomena associated with the transition. However, precise calculation of the critical exponents based on the Chalker-Coddington model remains challenging. The values of critical exponents are vital in the context of universality, wherein critical exponents are fixed constants representative of a broader universality class, defined via symmetries present in the model. In particular, the critical exponent governing the localisation length, ν has received much attention, with numerous estimations being made. Many of the estimations based on computational and theoretical models find differing values of ν which collectively do not coincide with experimental findings. Thus, in this thesis we investigate this discrepancy by using a real-space renormalisation group technique to calculate ν. In addition, the role of geometric disorder is considered via its implementation into the renormalisation scheme. We vary the amount of geometric disorder in the Chalker-Coddington model and study the effects on ν, comparing our numerical results against previous literature. The Chalker-Coddington model is then extended to a time-reversal invariant regime which describes the quantum spin-Hall effect and a renormalisation group transformation is successfully found.

Abbreviations

RG Renormalisation Group 22

RSRG Real-Space Renormalisation Group 22

FP Fixed Point 27

TRI Time-Reversal Invariant 10

Chapter 1

Introduction

In this chapter, we introduce the relevant Hall phenomena investigated throughout this thesis, joined with the background material required to give context and further understanding of the results discussed in later sections. We start with a brief primer on the classical Hall effect, which sets the foundations for the measured quantities in the classical regime. Immediately after, we take two separate approaches to the quantum Hall effect and provide an explanation for the most striking of phenomena subsequently found. We link a straightforward model describing the motion of an electron within the formalism of quantum mechanics to the degeneracy found at the resistivity plateaus. Secondly, we explore the role of topology in condensed matter physics, linking the Berry phase to the Chern number before discussing what it represents from the mathematical perspective. We find a form of the quantum Hall conductivity in terms of the Chern number, thereby linking the two. Time-reversal symmetry is additionally considered to provide a background for what will later be used in this thesis. We conclude by discussing critical exponents, universality and the success of renormalisation techniques in condensed matter physics.

1.1 A Brief Introduction to the Classical Hall Effect

To emphasise the unconventional properties of the quantum Hall effect and give the relevant experimental variables a clear introduction, we shall first consider the *classical Hall effect*. In his famous volumes on electromagnetism, Maxwell claimed that when exposed to a magnetic field, it is not the electrical current which experiences a resulting force, but the current-carrying conductor as a whole [1]. Upon reading this, Edwin H. Hall disputed Maxwell's claim and sought to investigate whether it was accurate. To do so, Hall designed an experiment involving a thin strip current-carrying conductor and a perpendicular magnetic field penetrating the sample [2]. Hall found that within the sample, the path of current flowing through the conductor is altered by the presence of the magnetic field, thus confirming his claim over Maxwell's. Furthermore, a potential transverse to the sample was detected. This transverse potential is dubbed the Hall potential.

To understand the origin of this potential we can first consider free electrons with mass m and charge e as kinetic point particles moving at velocity $\mathbf{v}$. When subjected to a magnetic field $\mathbf{B}$, the motion of a point negative charges follow

$$m\frac{d\mathbf{v}}{dt} = -e\mathbf{v} \times \mathbf{B}, \tag{1.1}$$

where t denotes time. For a constant magnetic field in a single direction, this differential equation is immediately solvable and solutions are found to be circular and exhibit typical cyclotron motion with angular frequency [3]

$$\omega = \frac{eB}{m}. \tag{1.2}$$

Building on this, we append the relevant terms relating to the Hall experiment. Hence, consider both a driving electric field $\mathbf{E}$ along the sample and a Drude term [4] owing to the approximation of electrons scattering to $\mathbf{0}$ momentum after a characteristic τ scattering time [5]. The $\mathbf{E}$ field contributes $-e\mathbf{E}$ to the force, while *Drude theory* provides the scattering term $\frac{m\mathbf{v}}{\tau}$ [4]. With this in mind, the equation of motion of electrons within the hall sample becomes

$$m\frac{\mathrm{d}\mathbf{v}}{\mathrm{d}t} = -e(\mathbf{E} + \mathbf{v} \times \mathbf{B}) - \frac{m\mathbf{v}}{\tau}. \tag{1.3}$$

The solutions to this equation no longer exhibit simple cyclotron motion due to the additional terms. Instead, we find that the Lorentz force $= q(\mathbf{E} + \mathbf{v} \times \mathbf{B})$ originating in the interaction between the magnetic and electric fields results in an

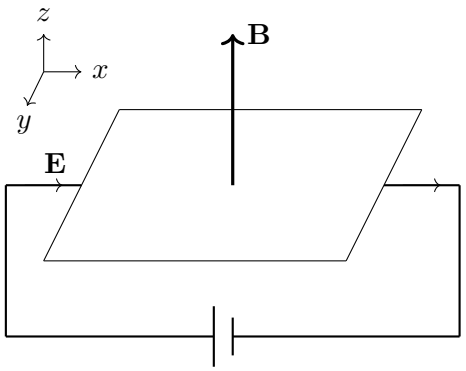

Figure 1.1: A diagram of a rectangular 2D Hall sample with **E** field pointing along the sample in the positive x direction and **B** field perpendicular to the sample in the positive z direction.

initial bias of electrons to one side of the sample. In effect, the sample experiences an initial accumulation of negative charge on one side and thus a net positive charge along the other. An attractive electric field $\mathbf{E}_b$ is produced between the two sides which counteracts the Lorentz force and in equilibrium, these two fields cancel out. Additionally, in equilibrium we must have $\frac{\mathrm{d}\mathbf{v}}{\mathrm{d}t} = 0$ and further, the component of the velocity transverse to the sample, $v_y = 0$. If otherwise $v_y \neq 0$ in equilibrium, electrons would be continually leaving the sample. Because the $\mathbf{B} = (0, 0, B)$ field only acts in one direction, we can simplify the vector expression in terms of vector components to

$$\frac{mv_x}{\tau} = -eE_x - ev_yB, \tag{1.4a}$$

$$\frac{mv_y}{\tau} = -eE_y + ev_xB. \tag{1.4b}$$

We can rearrange these two equations in terms of v_x and v_y so that

$$v_x = -\frac{e\tau E_x}{m} - \omega v_y\tau = -\frac{e\tau E_x}{m}, \tag{1.5a}$$

$$v_y = -\frac{e\tau E_y}{m} + \omega v_x\tau = 0. \tag{1.5b}$$

Now due to the simplifications present in our system, we have gone from two coupled equations in 1.4 to a more straightforward relation. We can rearrange in terms of the transverse electric field E_y to see that

$$E_y = \frac{m\omega v_x}{e}, \tag{1.6}$$

and so naturally we can evaluate a transverse potential difference as

$$V_H = -\int_0^w E_y \, \mathrm{d}y = \frac{m\omega v_x w}{e}, \tag{1.7}$$

where w is the width of the sample. While this gives ample explanation for the existence of transverse potential as originally detected by Hall, it is not the property we will be most interested in when moving to the quantum analogue of the classical Hall effect. In the quantum regime it is not the Hall potential which features the most striking properties, but the values of resistance measured both along and across the sample when varying the penetrating **B** field. We will thus identify the resistance for the classical case, before moving onto the quantum case.

Our first step is to start with an expression for the current density **J** in terms of the single electron velocity **v**

$$\mathbf{J} = -n_e e \mathbf{v}, \tag{1.8}$$

where n_e is the number of electrons flowing through the sample. While Drude theory is derived for the scenario of a single electron, it may seem odd to simply multiply the velocity of a single electron by how many electrons there are, as surely **v** is not entirely uniform across every electron. We can resolve the issue presented by noticing we can replace the **v** of a single electron with the group velocity of the whole Fermi sea where Drude theory still applies, albeit in a different frame [5]. From now on **v** will refer precisely to the group velocity. Additionally, we will use m^*, the effective mass, in place of the electron mass. If we rearrange (1.4) to

$$\frac{m^*}{\tau} v_x + eBv_y = -eE_x, \tag{1.9a}$$

$$\frac{m^*}{\tau} v_y - eBv_x = -eE_y, \tag{1.9b}$$

we can express the system in matrix form,

$$\begin{pmatrix} \frac{m^*}{\tau} & eB \\ -eB & \frac{m^*}{\tau} \end{pmatrix} \mathbf{v} = -e\mathbf{E}. \tag{1.10}$$

If we bring all the constants to one side we see that

$$\frac{m^*}{e^2 n_e \tau} \begin{pmatrix} 1 & \frac{eB\tau}{m^*} \\ -\frac{eB\tau}{m^*} & 1 \end{pmatrix} \mathbf{J} = \mathbf{E}. \tag{1.11}$$

Now we consider Ohm's law $\mathbf{J} = \sigma\mathbf{E}$, where σ represents the conductivity. What we seek with this derivation is the resistivity $\rho = \sigma^{-1}$ and so we have

$$\rho = \frac{m^*}{e^2 n_e \tau} \begin{pmatrix} 1 & \frac{eB\tau}{m^*} \\ -\frac{eB\tau}{m^*} & 1 \end{pmatrix}. \tag{1.12}$$

What this means is the *longitudinal resistivity* is

$$\rho_{xx} = \frac{m^*}{e^2 n_e \tau}, \tag{1.13}$$

while the transverse, or *Hall resistivity* becomes

$$\rho_{xy} = \frac{B}{e n_e}. \tag{1.14}$$

What we have shown is that the Hall resistivity is linear in magnetic field, showing the penetrating $\mathbf{B}$ field incites transverse motion in the electrons [4]. For completion, we will additionally derive forms for the conductivity in terms of the resistivity as they make future derivations clearer. To arrive at the conductivity as $\sigma = \rho^{-1}$ we can simply matrix invert to find

$$\sigma = \frac{1}{\rho_{xx}^2 + \rho_{xy}^2} \begin{pmatrix} \rho_{xx} & -\rho_{xy} \\ \rho_{xy} & \rho_{xx} \end{pmatrix}. \tag{1.15}$$

1.2 The Quantum Hall Effect

With this knowledge of classical Hall resistivity measurements in mind, we can move onto discussing the *quantum Hall effect*. As with many interesting phenomena within condensed matter physics, the propensity for a sample to exhibit effects inexplicable by classical physics increases at lower temperatures [6]. At temperatures close to zero, dephasing of the microscopic wavefunction becomes negligible, allowing for a coherent wavefunction to exhibit phenomena particular to the quantum regime [7]. The quantum Hall effect is no exception. With a sample cooled to around 1K and the $\mathbf{B}$ field in the order of 10T, in 1980, Klaus von Klitzing et al [8] discovered behaviour of the sample resistivity to deviate from what was previously found classically. With a sample prepared as described, instead of a linear relationship between magnetic field strength and transverse Hall resistivity, a full quantization was observed in units of $\frac{e^2}{h}$, see figure 1.2. More precisely this effect may be referred to as the *integer* quantum Hall effect as the quantisation is limited to integers. The *fractional* quantum Hall effect is briefly discussed in section 1.5 however henceforth,

when referring to the quantum Hall effect, we only consider the integer effect. As a consequence of the quantisation, the observations by von Klitzing allowed for an accurate calculation of the fine structure constant $\alpha = \frac{e^2}{2\epsilon_0 ch}$. An astounding property of the quantisation of resistivity is that weak disorder manifested through either geometric, electric or material impurities has no bearing on the precision of the quantisation. In fact, weak disorder present in the sample generates more states for electrons to localise to (see section 1.2.2), and results in broader observed plateaux (within reason) [9]. The effect on the plateaux width is shown in figure 1.3. The particular protection from weak disorder inherent to the quantum Hall effect will be explored later in this project with the introduction of geometric disorder to the model. The counterintuitive nature of the quantum Hall effect does not end there; unlike many other examples in quantum mechanics where quantisation is a direct result of symmetry, the quantisation of the quantum Hall effect arises due to topological effects [10]. Before we examine the topological aspects of the quantum Hall effect, we shall first give a strictly quantum mechanical argument behind the bulk phenomena.

1.2.1 Quantum Mechanical Approach

The Drude model as posed before will not suffice in the following derivation. We will be considering the quantised energy levels available to the electrons which the Drude model cannot account for. We will thus use a quantum Hamiltonian H to describe the dynamics of the electron. In a $\mathbf{B}$ field we can write H in terms of the momentum and vector potential operators, $\hat{\mathbf{p}}$ and $\hat{\mathbf{A}}$ respectively. In SI units with c being the speed of light we write the Hamiltonian as [14]

$$\hat{H} = \frac{1}{2m}(\hat{\mathbf{p}} + \frac{e}{c}\hat{\mathbf{A}})^2, \tag{1.16}$$

from which we will derive solutions to the corresponding time-independent Schrödinger equation for wavefunctions $|\psi\rangle$ and eigenenergies E,

$$\hat{H}|\psi\rangle = E|\psi\rangle. \tag{1.17}$$

In this scenario, it is most useful to take the Landau gauge: $\hat{\mathbf{A}} = xB\hat{\mathbf{y}}$, with x denoting the distance along the sample in the direction of the $\mathbf{E}$ field. We can now give more detail to our Hamiltonian by writing in terms of the operator components

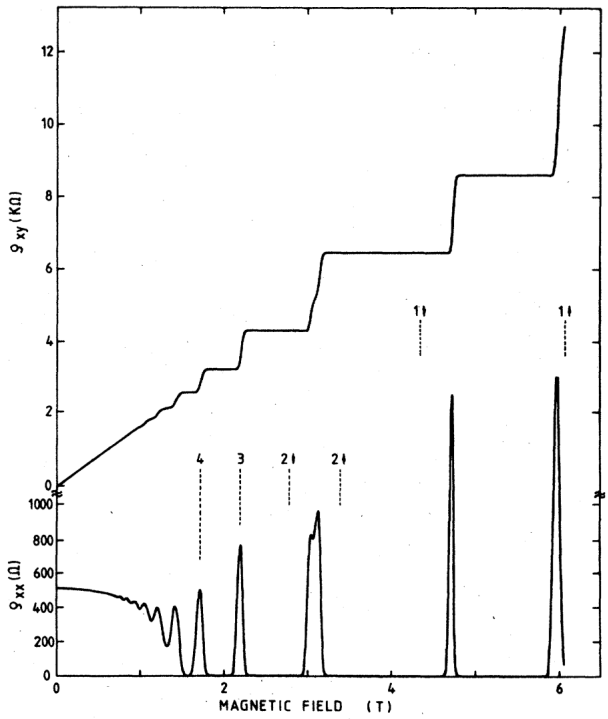

Figure 1.2: Experimental measurements of the longitudinal resistivity ρ_{xx} and the transverse resistivity ρ_{xy} taken from a quantum Hall sample against a varying **B** field between 0 and 6T. Taken from reference [11].

$\hat{p}_x$ and $\hat{p}_y$, neglecting $\hat{p}_z$ as the electrons lie within two dimensions only, so that

$$\hat{H} = \frac{1}{2m}\Big[\hat{p}_x^2 + (\hat{p}_y + \frac{eB}{c}\hat{x})^2\Big]. \tag{1.18}$$

We suppose a translational symmetry in the **y** direction (by wrapping the sample into a cylinder) and so we are at liberty to apply a separation of variables solution. If we take the step to write our wavefunction as

$$\psi_k(x, y) = e^{iky} f_k(x), \tag{1.19}$$

for some wavenumber k, then our wavefunction is an eigenstate of the momentum in the **y** direction. When substituted back into the Hamiltonian, we recast the problem as finding a solution for x given k as

$$h_k f_k(x) = \frac{1}{2m_e}\Big[\hat{p}_x^2 + (\hbar k - \frac{eB}{c}x)^2\Big] f_k(x) = E_k f_k(x), \tag{1.20}$$

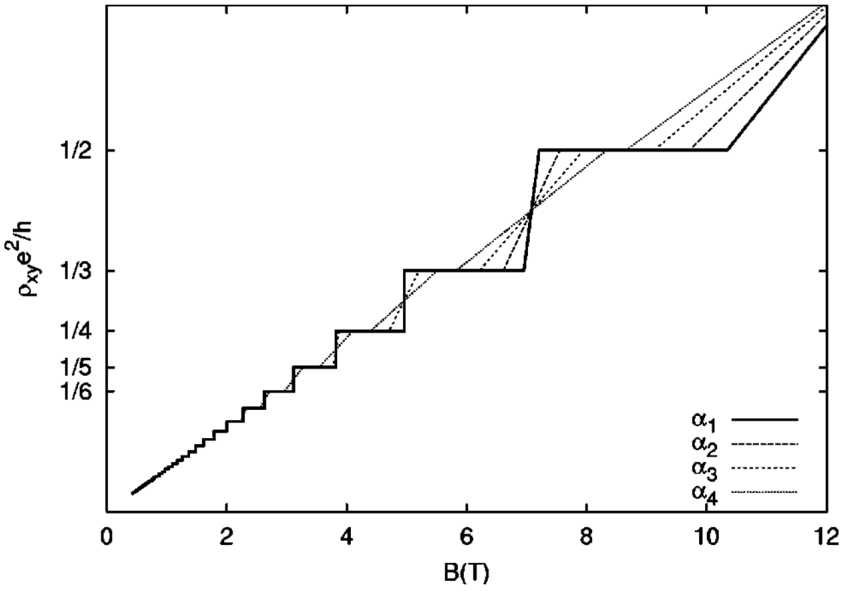

Figure 1.3: Theoretical predictions of the ρ_{xy} against B curve for different levels of impurity-driven disorder. The lines are indexed by α, with a larger index indicating a smaller presence of disorder. Image taken from [12]. Experimental observation of this phenomenon is detailed in [13].

where h_k refers to the Hamiltonian acting only on the x dependent part of ψ. From here we can spot the similarity with the quantum harmonic oscillator [15], especially as we can group constants together and see that

$$h_k = \frac{\hat{p}_x^2}{2m_e} + \frac{1}{2}m_e\omega_c^2(x - k\ell^2)^2, \tag{1.21}$$

where we have introduced the cyclotron frequency $\omega_c = \frac{eB}{cm}$ and the magnetic length $\ell = \sqrt{\frac{\hbar c}{eB}}$ to further clarify the harmonic oscillator form of h_k. For any k, we then specify a guiding centre for which there exists a set of harmonic oscillator energy eigenvalues

$$E_{n_L} = \hbar\omega_c\Big(n_L + \frac{1}{2}\Big), \tag{1.22}$$

and our eigenfunctions will be composed of the plane wave in the **y** direction, as well as typical Hermite polynomials together with a Gaussian in the **x** direction [15]. Explicitly the unnormalized eigenfunction will be

$$\psi_{n_L k}(x, y) = e^{iky}H_{n_L}\left(\frac{x}{\ell} - k\ell\right)\exp[-\frac{1}{2\ell^2}(x - k\ell^2)^2]. \tag{1.23}$$

Thanks to the rather strongly converging Gaussian in (1.23), these wavefunctions are quite severely localised, and thus each n_L energy level holds a rather large degeneracy. If the wavefunctions were not localised, the Pauli exclusion principle would prohibit the electrons from inhabiting the same energy level, but due to the localisation, multiple wavefunctions can exist in separate areas of the sample at the same energy level, while being unaffected by Pauli exclusion. In fact, for each energy level there exists $N = \frac{eBA}{2\pi\hbar}$ degenerate states [6], where A denotes the area of the sample. These degenerate energy levels are called *Landau levels* [16] and these describe the energies associated with each resistivity plateau. While we have imposed a significant amount of simplifications upon the system, even with only a few simple considerations, we have uncovered the sharp quantisation of the energy levels of the electrons.

1.2.2 Disorder

It would be remiss not to appreciate the role of *disorder* in the manifestation of the quantum Hall effect. Indeed the Chalker-Coddington model (2) which we extensively use throughout this thesis is in essence an abstraction of a disordered 2D potential. In many quantum systems, the impact of disorder can become an obstacle to any particular phenomena being realised in an experimental setup. Examples including background noise affecting resistance measurements and impurities diminishing the ability for a sample to superconduct [17] all point to the profound importance of disorder. However, disorder is not only a mechanism of obfuscating certain phenomena; disorder can become a necessity in the manifestation of quantum phenomena, such as the quantum Hall effect. As discussed in the beginning of 1.2, it is the disorder throughout the system which drives the localisation of electrons and permits the large degeneracy needed for stable Hall plateaux. Prior to the discovery of the quantum Hall effect, in a widely influential paper by Anderson [18], the localisation effect of 2D disorder was examined and thereafter thoroughly studied by many others [19]. Named after the author, the theory of *Anderson localisation* is a cornerstone upon which the theory of the integer quantum Hall effect rests. When considering the scaling phenomena, and ultimately deriving the critical exponent ν from the Chalker-Coddington model, the application of the disorder driven Anderson localisation transition forms the foundation of our analysis.

1.3 Origin of Topology in Physical Systems

In this section we will give an introduction to the role of *topology* within the quantum Hall effect, and how it can give a satisfactory explanation for the strict quantisation observed in the quantum Hall effect, how topology can relate the phenomena of the bulk of the sample to the edge and how related ideas can explain the existence of a quantum Hall effect in the absence of a magnetic field. In the broader context of physics in general, concepts of symmetry provide us myriad of phenomena [20–23]. From conservation of angular momenta leading to quantisation in small quantum systems [15], to spontaneous $U(1)$ symmetry breaking leading to the ferromagnetic phase transition [24], an understanding of symmetry underpins a thorough understanding to a startling amount of physics. Despite this, there are some ideas in physics more satisfactorily explained by ideas from topology, not symmetry [25]. In this section, we introduce the Berry phase, a consequence of the adiabatic theorem, and what it can tell us about the system considered. We will then link the Berry phase to the Chern number, a topological invariant which takes integer values depending on the values of the Berry phase. Our next step will be to link the Chern number to the conductance of our quantum Hall system, thereby closing the loop and providing us with a topological explanation for the quantisation of Hall resistivity. It is interesting to note that the first topological explanation given for the quantum Hall effect made no use of Chern numbers or Berry phases. Instead, Thouless, Kohmoto, Nightingale and den Nijs considered solutions to Harper's equation for rational flux quanta per unit cell [26]. These solutions were found to be restricted to a Diophantine equation dependent only on the topology of the sample, which specified the Hall conductance at integer values. At the end of this section we will introduce the *Time-Reversal Invariant (TRI)* extension of the quantum Hall effect, in which the magnetic field is absent, yet interactions between spins form the basis of a quantum spin Hall effect.

1.3.1 All Things Berry

In standard treatments of simple quantum mechanical systems, we are given a Hamiltonian which acts on a wavefunction which is itself parameterised by a set of coordinates (such as position, momentum or time). In this formalism, the Hamiltonian itself is not considered to change. Here we are describing the Schrödinger picture which makes our argument clearer, but what follows is equally true for the Heisenberg picture. The invariance of the Hamiltonian is based upon variables latent to the system, although external variables such as experimental details may

still vary the Hamiltonian, irrespective of the Schrödinger or Heisenberg picture. So in addition to the collection of wavefunctions being drawn from Hilbert space, we can specify a parametrisation of the Hamiltonian which may produce a slightly varying set of eigenstates depending on the parameters. Let us propose that we possess a Hamiltonian which is specified by external parameters $\mathbf{R}(t)$ which themselves depend on time t. We denote the Hamiltonian

$$H = H[\mathbf{R}(t)]. \tag{1.24}$$

Now we consider the eigenstates of such a Hamiltonian as $\mathbf{R}$ varies. As previously mentioned, the parameters specifying the Hamiltonian may indeed alter the set of eigenstates. Following from this, we have the parameterised Schrödinger equation

$$H[\mathbf{R}(t)]|n[\mathbf{R}(t)]\rangle = E_n[\mathbf{R}(t)]|n[\mathbf{R}(t)]\rangle, \tag{1.25}$$

where $|n\rangle$ are the n eigenstate solutions to the Hamiltonian. What the adiabatic theorem tells us about these eigenstates is that eigenstates from one Hamiltonian specified by $\mathbf{R}(t_1)$ will be mapped to the corresponding eigenstate from the Hamiltonian specified by $\mathbf{R}(t_2)$, as long as the Hamiltonian varies between $\mathbf{R}(t_1)$ and $\mathbf{R}(t_2)$ sufficiently slowly [27]. After this transformation, while we know what eigenstate we may be in, it is prudent to remember that the evolution in a particular eigenstate requires only that $|\psi(t_2)|^2 = |\psi(t_1)|^2$. Consequently, there exists a gauge freedom of some phase, as of yet undetermined [28]. As the energy eigenvalues themselves also depend on $\mathbf{R}$, we can expect to gain a dynamical phase [6]. Surprisingly, that is not the only factor, as the resulting phase is derived from both the dynamical phase and a separate quantity known as a geometric phase [29]. Intuitively, the geometric phase represents how much a vector 'twists' as it evolves along a closed path via parallel transport [30]. This is purely geometric and depends on the shape of the parameter space $\mathbf{R}(t)$ specifying the Hamiltonian for any t. To see this we can explicitly take a wavefunction $|\psi(t)\rangle = e^{-i\theta(t)}|n[\mathbf{R}(t)]\rangle$ to have the phase accounted for, and apply this form to the Schrödinger equation

$$H[\mathbf{R}(t)]e^{-i\theta(t)}|n[\mathbf{R}(t)]\rangle = i\hbar\frac{\mathrm{d}}{\mathrm{d}t}\Big\{e^{-i\theta(t)}|n[\mathbf{R}(t)]\rangle\Big\}, \tag{1.26}$$

which with a modest application of the product rule leaves us with

$$e^{-i\theta(t)}E_n[\mathbf{R}(t)]|n[\mathbf{R}(t)]\rangle = i\hbar e^{-i\theta(t)}\left\{\frac{\mathrm{d}\theta(t)}{\mathrm{d}t}|n[\mathbf{R}(t)]\rangle + \frac{\mathrm{d}}{\mathrm{d}t}|n[\mathbf{R}(t)]\rangle\right\}. \tag{1.27}$$

By multiplying with $\langle n(\mathbf{R}(t)|$ and simplifying we then see that

$$E_n[\mathbf{R}(t)] = i\hbar\langle n[\mathbf{R}(t)]|\frac{\mathrm{d}}{\mathrm{d}t}|n[\mathbf{R}(t)]\rangle + \hbar\frac{\mathrm{d}\theta(t)}{\mathrm{d}t}. \tag{1.28}$$

All we have to do here is rearrange for $\theta(t)$ and find

$$\theta(t) = \frac{1}{\hbar}\int_0^{t'} E_n[\mathbf{R}(t)]\,\mathrm{d}t - i\int_0^{t'}\langle n[\mathbf{R}(t)]|\frac{\mathrm{d}}{\mathrm{d}t}|n[\mathbf{R}(t)]\rangle\,\mathrm{d}t, \tag{1.29}$$

which as previously mentioned, contains the dynamical phase generated from the energy eigenvalues, alongside a geometric term. Taking advantage of the geometric origin, we can release ourselves from strict dependence on time as the parameters $\mathbf{R}$ already have a time dependence. Hence, by a change of coordinates (and a change from a regular integral to a line integral in parameter space) we define the *Berry phase* as [29]

$$\zeta_n = i\int_{\mathcal{C}}\langle n(\mathbf{R})|\nabla_{\mathbf{R}}|n(\mathbf{R})\rangle\,\mathrm{d}\mathbf{R}. \tag{1.30}$$

This definition can be used to additionally define the *Berry connection* [31], which is simply the integrand of the Berry phase in (1.30) and can be thought of as our means of parallel transport along parameter space, as mentioned earlier. Thus, the Berry connection is

$$\mathbf{A}_n = i\langle n(\mathbf{R})|\frac{\partial}{\partial\mathbf{R}}|n(\mathbf{R})\rangle. \tag{1.31}$$

Directly from this definition, we can introduce the *Berry curvature*, which is the curvature form for the parameter space we are working in. This status as a curvature form will be crucial in the next section. We define it as

$$\mathbf{\Omega}_n = \nabla_{\mathbf{R}} \times \mathbf{A}_n(\mathbf{R}). \tag{1.32}$$

While not explicitly seen in the derivation, it is still valuable to point out the gauge-dependent properties of these three quantities. When integrated over a closed path, the Berry phase is gauge independent and thus manifests in physical phenomena. In contrast, the Berry connection at any particular point (or along any open path) is gauge dependent and so of no meaning to us alone. The Berry curvature is another method of eliminating the gauge dependence of the Berry connection, similar to how the magnetic vector potential loses its gauge dependence upon the curl operator being applied [32].

1.3.2 The First Chern Number

So far what we have seen is securely rooted in physics, but now we will see the link to why the word 'topological' is used to describe these quantum Hall states. What follows is a discussion of mathematical ideas, albeit far removed from rigour in an effort to convey the necessary ideas for a motivated explanation for quantum Hall physics. In a study of complex vector bundles, Chern found multiple ways of expressing a topological invariant which grouped the complex vector bundles into characteristic classes [33]. In the broader field of topology, a topological invariant is any quantity or Boolean property that can be found for a particular topological space, which characterises and classifies that particular topological space in distinction with others [34]. In our context, a vector bundle is composed of any general space which at each point is equipped with a vector space [35]. A complex vector bundle is precisely a vector bundle for which the vector spaces are defined over the complex numbers. This mathematical construct is exactly what we started with in the previous section! Our general space is the parameter space specifying the Hamiltonian, with each Hamiltonian equipped with slightly differing vector spaces of wavefunctions. This is the crucial link which allowed for the application of Chern's work to condensed matter systems. Chern created characteristic classes which act as topological invariants for complex vector bundles. Out of the numerous formulations of the Chern classes [33], the implementation most accessible to us is via differential geometry. In terms of differential forms on the manifold, the n_cth Chern class can be computed via an expression involving the curvature form of the vector bundle [35]. Now there are a couple of important facts before we bring this back to the physics. Firstly, in all situations useful to us, all Chern classes above the first vanish[35]. Secondly, the top Chern class is equivalent to the Euler class for the underlying real vector bundle [36]. The Euler class is a separate topological invariant defined only on real vector bundles, but the equivalence in this situation is what will allow us direct computation of the Chern number. To finally form an expression from the preceeding arguments we use the Chern-Gauss-Bonnet theorem. The Gauss-Bonnet theorem links the curvature of a 2 dimensional compact manifold to the Euler characteristic χ. Chern generalised the theorem to a much broader class of manifolds, although more importantly for our situation derived a particular form relating the Euler class $\mathfrak{e}$ to χ [37]. Explicitly, the theorem states that

$$\chi(M) = \int_M \mathfrak{e}(\Omega), \tag{1.33}$$

where M denotes the manifold and Ω denotes the curvature form defined on the manifold. The Euler class, $\mathfrak{e}(\Omega)$ is separately evaluated as

$$\mathfrak{e}(\Omega) = \frac{1}{(2\pi)^{\frac{m}{2}}}\mathrm{Pf}(\Omega). \tag{1.34}$$

where $\mathrm{Pf}(\Omega)$ is the Pfaffian of the curvature form [38]. Once again things can simplify since we will be working only in 2 dimensions. The Pfaffian of the most general skew-symmetric matrix in 2 dimensions is merely the single degree of freedom permitted and so it simplifies to Ω. With $m = 2$ we find that

$$\chi(M) = \frac{1}{2\pi}\int_M \Omega. \tag{1.35}$$

Due to the equivalence particular to our situation between the Euler class and the top Chern class, we can also call the Euler characteristic the Chern number. As we set out to find, the Chern number is a topological invariant and more importantly, because of the Chern-Gauss-Bonnet theorem, is strictly an integer.

1.3.3 The Chern Number and the Quantum Hall Conductivity

Now that we have clarified the mathematical perspective, we have found a formula for a topological invariant quantised to integer values in terms of an integral over a curvature form. Now we shall apply this to the quantum Hall effect. In place of the general curvature form Ω we place our Berry curvature (1.32), and for our manifold we have a 2-dimensional Brillouin zone in terms of k_x and k_y. We then make the further clarification that in the following expressions, the Berry connection is automatically summed across all filled bands. We define the Berry curvature on each band in the Brillouin zone, as can be noted from the eigenstate dependence of the Berry connection (1.31). We find an expression for the *Chern number* describing the topology of the first Brillouin zone in terms of the Berry curvature

$$\chi = C = \frac{1}{2\pi}\iint_{\mathbf{k}\in 1\mathrm{BZ}} \Omega\,\mathrm{d}k_x\mathrm{d}k_y. \tag{1.36}$$

Because of our restriction to 2 dimensions, the Berry curvature itself simplifies to

$$\Omega(\mathbf{k}) = \frac{\partial A_y(\mathbf{k})}{\partial k_x} - \frac{\partial A_x(\mathbf{k})}{\partial k_y}. \tag{1.37}$$

We are yet to make the connection from any of the above expressions to the quantum Hall conductivity. To begin making the connection we start by once again

considering the time independent Schrödinger equation

$$H(\mathbf{k})|n(\mathbf{k})\rangle = E_n(\mathbf{k})|n(\mathbf{k})\rangle. \tag{1.38}$$

We take the derivative with respect to k_x, so that

$$\frac{\partial}{\partial k_x}\Big[H(\mathbf{k})|n(\mathbf{k})\rangle\Big] = \frac{\partial}{\partial k_x}\Big[E_n(\mathbf{k})|n(\mathbf{k})\rangle\Big], \tag{1.39}$$

which expands to

$$\frac{\partial H(\mathbf{k})}{\partial k_x}|n(\mathbf{k})\rangle + H(\mathbf{k})\frac{\partial}{\partial k_x}|n(\mathbf{k})\rangle = \frac{\partial E_n(\mathbf{k})}{\partial k_x}|n(\mathbf{k})\rangle + E_n(\mathbf{k})\frac{\partial}{\partial k_x}|n(\mathbf{k})\rangle. \tag{1.40}$$

From here we can take the inner product with the state $\langle n'(\mathbf{k})|$ so that

$$\langle n'(\mathbf{k})|\frac{\partial H(\mathbf{k})}{\partial k_x}|n(\mathbf{k})\rangle = E_n(\mathbf{k})\langle n'(\mathbf{k})|\frac{\partial}{\partial k_x}|n(\mathbf{k})\rangle - \langle n'(\mathbf{k})|H(\mathbf{k})\frac{\partial}{\partial k_x}|n(\mathbf{k})\rangle, \tag{1.41a}$$

$$= [E_n(\mathbf{k}) - E_{n'}(\mathbf{k})]\langle n'(\mathbf{k})|\frac{\partial}{\partial k_x}|n(\mathbf{k})\rangle. \tag{1.41b}$$

In finding (1.41a) from (1.40) we note that $\frac{\partial E_n(\mathbf{k}}{\partial k_x}\langle n'(\mathbf{k})|n(\mathbf{k})\rangle = 0$. With an identical derivation, we can find the following expression involving k_y,

$$\langle n(\mathbf{k})|\frac{\partial H(\mathbf{k})}{\partial k_y}|n'(\mathbf{k})\rangle = [E_n(\mathbf{k}) - E_{n'}(\mathbf{k})]\langle\frac{\partial}{\partial k_y}n(\mathbf{k})|n'(\mathbf{k})\rangle. \tag{1.42}$$

We then multiply these expressions together to find

$$\langle n(\mathbf{k})|\frac{\partial H(\mathbf{k})}{\partial k_y}|n'(\mathbf{k})\rangle\langle n'(\mathbf{k})|\frac{\partial H(\mathbf{k})}{\partial k_x}|n(\mathbf{k}), \tag{1.43}$$

$$= [E_n(\mathbf{k}) - E_{n'}(\mathbf{k})]^2\langle n(\mathbf{k})|\frac{\partial}{\partial k_y}|n'(\mathbf{k})\rangle\langle n'(\mathbf{k})|\frac{\partial}{\partial k_x}|n(\mathbf{k})\rangle.$$

If we rearrange the expression and sum over the n' index and note the resolution of the identity $\sum_{n'}|n'(\mathbf{k})\rangle\langle n'(\mathbf{k})| = \mathbb{I}$ then we can see that

$$\sum_{n\neq n'}\frac{\langle n(\mathbf{k})|\frac{\partial H(\mathbf{k})}{\partial k_y}|n'(\mathbf{k})\rangle\langle n'(\mathbf{k})|\frac{\partial H(\mathbf{k})}{\partial k_x}|n(\mathbf{k})\rangle}{[E_n(\mathbf{k}) - E_{n'}(\mathbf{k})]^2} = \sum_{n\neq n'}\langle\frac{\partial}{\partial k_y}n'(\mathbf{k})|n'(\mathbf{k})\rangle\langle n'(\mathbf{k})|\frac{\partial}{\partial k_x}n'(\mathbf{k})\rangle \tag{1.44a}$$

$$= \sum_{n'}\langle\frac{\partial}{\partial k_y}n'(\mathbf{k})|\frac{\partial}{\partial k_x}n'(\mathbf{k})\rangle. \tag{1.44b}$$

Our goal in this derivation is to link the Berry curvature to the Hall conductivity and so far we have an expression which has linked to neither. From here we will link one side to the Chern number and the other to the Hall conductivity, thereby bridging the gap. The link to the Berry curvature (1.37) arrives swiftly when we see from the RHS of (1.44b) that

$$\sum_{n'}\langle\frac{\partial}{\partial k_y}n'(\mathbf{k})|\frac{\partial}{\partial k_x}n'(\mathbf{k})\rangle=\frac{\partial}{\partial k_y}\langle n'(\mathbf{k})|\frac{\partial}{\partial k_x}|n'(\mathbf{k})\rangle=\frac{1}{i}\frac{\partial A_x}{\partial k_y}. \tag{1.45}$$

By taking the complex conjugate of the expression, we retrieve something similar involving $\frac{\partial A_y}{k_x}$ and by combining those expressions we find the Berry curvature (1.37)

$$\Omega(\mathbf{k})=i\sum_{n\neq n'}\frac{\langle n(\mathbf{k})|\frac{\partial H(\mathbf{k})}{\partial k_y}|n'(\mathbf{k})\rangle\langle n'(\mathbf{k})|\frac{\partial H(\mathbf{k})}{\partial k_x}|n(\mathbf{k})\rangle-\text{c.c.}}{[E_n(\mathbf{k})-E_{n'}(\mathbf{k})]^2}. \tag{1.46}$$

Now the last step is to link this to the Hall conductivity. From linear response theory, the *Kubo formula* can be derived for the quantum Hall conductivity σ_{xy} [26]. It is shown to take the form

$$\sigma_{xy}=\frac{ie^2}{\hbar}\sum_{\mathbf{k}}\sum_{n\neq n'}\frac{\langle n(\mathbf{k})|\frac{\partial H(\mathbf{k})}{\partial k_y}|n'(\mathbf{k})\rangle\langle n'(\mathbf{k})|\frac{\partial H(\mathbf{k})}{\partial k_x}|n(\mathbf{k})\rangle-\text{c.c.}}{[E_n(\mathbf{k})-E_{n'}(\mathbf{k})]^2}. \tag{1.47}$$

The substitution required is clear from inspection and so finally, we identify

$$\sigma_{xy}=\frac{e^2}{\hbar}\frac{1}{(2\pi)^2}\iint_{\mathbf{k}\in 1\text{BZ}}\Omega(\mathbf{k}),\mathrm{d}k_x\mathrm{d}k_y, \tag{1.48}$$

and

$$\sigma_{xy}=\frac{e^2}{h}C. \tag{1.49}$$

We have completed the link from Berry phase to Hall conductivity. *This* is why the transverse conductivity of the quantum Hall effect is strictly quantised to integer multiples of $\frac{e^2}{h}$. Going between sections, we have switched from talking about the resistivity ρ_{xy} to the conductivity σ_{xy}. As we showed in equation (1.15), these are related by $\sigma_{xy}=\frac{\rho_{xy}}{\rho_{xx}^2+\rho xy^2}$. At each plateaus, $\rho_{xx}=0$, as is experimentally verified, leaving us with $\sigma_{xy}=\frac{1}{\rho_{xy}}$. We can conclude that our demonstration of conductivity quantisation implies resistivity quantisation. As we have found topological properties derived from the band structure of the system, the quantum Hall sample may be referred to as a *topological insulator*, due to its insulating bulk [39]. Specifically, as we use the Chern number as the topological invariant, we may also refer

to the quantum Hall sample as simply a *Chern insulator*. This nomenclature is not reflexive, as not all Chern insulators will necessarily be quantum Hall samples [40].

1.3.4 Edge States and the Bulk-Boundary Correspondence

Equation (1.23) tells us that the wavefunctions of the quantum Hall effect are localised in the x direction, but we also know that we have non-zero entries in the conductivity tensor. This would seem to be a contradiction, as localised states would not be expected to contribute to conductivity. We can reconcile this contradiction by considering the stark difference between the behaviour of the bulk of the sample and the edge of the sample. Furthermore, this contrasting phenomenon ties directly into the topological arguments presented thus far. The surprising resolution to this contradiction is that there exist *chiral edge states* which carry a current resulting in non-zero conductivity in spite of an insulating bulk [10]. The existence of such states is a direct corollary of the topological nature of the band structure. To change the Chern number of a 2D $\mathbf{k}$ torus necessarily means a discontinuous change into a different part of parameter space that is also insulating in the bulk. To progress from one insulating phase to another, a band crossing must occur. As the Chern number of free space is trivially 0, any non-zero Chern number in the bulk of the sample implies that at the boundary between spaces of differing Chern number, a band crossing must occur [31]. The amount of band crossings is equal to the amount of conducting modes at the edge. This in principle is the bulk-boundary correspondence and remains a hallmark of many topological systems [31]. These conducting edge states are chiral due to the magnetic field penetrating the sample, meaning that they all run either clockwise or anti-clockwise around the very edge of the sample.

1.4 The Quantum Spin Hall Effect

Our derivations so far made full utilisation of the B field as the primary driving force giving rise to quantum Hall physics. However, in particularly clean samples, it was predicted and subsequently demonstrated that in HgTe quantum wells, a quantum Hall state is still observed despite an absence of magnetic field [41–43]. Instead of the magnetic field, the spin-orbit coupling is responsible for the plateaus in conductivity [41]. This effect is hence called the *quantum spin-Hall effect*, although it may also be referred to as a TRI topological insulator, for reasons we will discuss. Throughout this thesis, the two terms are used interchangeably. Despite this change of driving force being the only main difference, there are some indirect consequences of which

an understanding will be useful to us later in this thesis.

1.4.1 Time-Reversal Symmetry

A natural consequence of the presence of a B field in the quantum Hall sample is the breaking of time-reversal symmetry. Time-reversal symmetry is a discrete symmetry such that the system maintains the same state under a reversal of time $t \mapsto -t$. In the context of observables relating to the Hamiltonian, the position is unchanged $\mathbf{x} \mapsto \mathbf{x}$ while the momentum flips its sign $\mathbf{p} \mapsto -\mathbf{p}$. If we applied a transformation that did just that and nothing more, the canonical commutation relation between $\mathbf{x}$ and $\mathbf{p}$ would no longer hold. To remedy this, we impose the additional condition that $i \mapsto -i$, i.e. complex conjugation. In mathematical terms, the time-reversal operator $\mathcal{T}$ is anti-unitary [44]. We can thus decompose $\mathcal{T}$ into

$$\mathcal{T} = UK, \tag{1.50}$$

where U represents a unitary operator, and K represents complex conjugation. We then can see that

$$\mathcal{T}^2 = UKUK = UU^* = e^{i\phi}\mathbb{I}, \tag{1.51}$$

as we retain gauge freedom when applying any unitary operator to our wavefunctions. This implies that

$$U = e^{i\phi}Ue^{i\phi}, \tag{1.52}$$

which gives us the necessary condition that $e^{i\phi} = \pm 1$ which further implies that $\mathcal{T}^2 = \pm 1$. In physical systems, due to how representations of the time-reversal operator form in conjunction with spin, particles of half-odd-integer spin exhibit $\mathcal{T}^2 = -1$ symmetry while particles of integer spin exhibit $\mathcal{T}^2 = 1$ [45]. This leads to the rather interesting result that for a fermion, one has to apply the time reversal operator 4 times in order to attain the original state. When we take $\mathcal{T}^2 = -1$, non-trivial consequences involving the eigenstate spectrum occur. Consider two separate eigenstates $|\varphi\rangle$ and $|\psi\rangle$, we find that

$$\langle \mathcal{T}\varphi | \mathcal{T}\psi \rangle = (U|\varphi\rangle^*)^\dagger U|\psi^*\rangle = |\varphi^*\rangle^\dagger U^\dagger U|\psi^*\rangle = \langle \varphi^*|\psi^*\rangle = \langle \varphi|\psi\rangle^*. \tag{1.53}$$

Now if we take $|\varphi\rangle = \mathcal{T}|\psi\rangle$ and apply the reverse of this equality we can find that:

$$\langle \mathcal{T}\psi|\psi\rangle^* = \langle \mathcal{T}^2\psi|\mathcal{T}\psi\rangle = -\langle \psi|\mathcal{T}\psi\rangle = -\langle \mathcal{T}\psi|\psi\rangle^*. \tag{1.54}$$

This necessarily means that $\langle \mathcal{T}\psi|\psi\rangle = -\langle \mathcal{T}\psi|\psi\rangle$, i.e. both $|\psi\rangle$ and $|\mathcal{T}\psi\rangle$ are orthogonal to each other while attaining the same energy eigenvalue. For a Hamiltonian possessing time-reversal symmetry while acting on fermions, a two-fold degeneracy will appear, corresponding to how each eigenstate has a time-reversed partner of equal eigenenergy. This is called a *Kramer's degeneracy* and is integral to our formulation of time-reversal symmetry in the model used within this thesis [45]. If instead we had specified $\mathcal{T}^2 = 1$, as is the case for bosons, no such degeneracy occurs. Following this, instead of chiral edge states running along the edge of the sample, a TR-invariant topological insulator has time-reversed copies running in opposite chirality of the normal time edge states. Similarly to the quantum Hall effect, a topological invariant can be derived. In the quantum spin Hall effect, this topological invariant is no longer any integer, instead it lies in $\mathbb{Z}_2$ and corresponds directly to the number of Kramer's pairs [31]. In other words, successive addition of Kramer's pairs changes the sample from being topologically trivial, to non-trivial, back to trivial and so on.

1.5 The Fractional Quantum Hall Effect

While this project is concerned with non-interacting models of the quantum Hall and quantum spin Hall effect, it would not be a complete presentation of quantum Hall effects without acknowledgement of the fractional case. Whilst for dirty samples in the range of up to 10T, the conductance plateaus are strictly quantised to integer multiples of $\frac{e^2}{h}$, this does not complete the entire picture of what can happen inside a quantum Hall sample. In 1982 Tsui et al found that in very clean samples, specifically at $B > 10$T, additional plateau started appearing [46]. Furthermore, the additional plateaux take on very specific rational, non-integer values, such as $\frac{1}{3}$ and $\frac{2}{5}$ [47]. These fractional states can only be explained by including interactions between electrons and result in predictions of corresponding fractionally charged electrons [48]. As exciting as this prospect may seem, theories explaining such states are far removed from the topic of this project and will no further be discussed.

1.6 The Critical Exponent

When one phase of matter changes into another, it is described as undergoing a *phase transition* [49]. One familiar example would be that of an Ising ferromagnet

in a 2-dimensional square lattice. The model was originally believed to be not analytically solvable. However, in 1944, Onsager published a stunning paper doing just that (for vanishing external field) [50]. This achievement is considered one of the biggest breakthroughs in statistical physics [51]. For a 2D Ising ferromagnet, we can slowly vary the temperature T, which at some critical threshold T_c abruptly alters the macroscopic properties of the system, changing between paramagnetic and ferromagnetic phases. On the microscopic level, this transition to the ferromagnetic phase from the paramagnetic phase is induced by a spontaneous uniform aligning of site spins, thus manifesting long range order. The origin of spontaneous alignment in 2D Ising electrons comes from a minimising of the coulomb and exchange interaction energies. To quantify how one phase shifts to another we can introduce an *order parameter*. By definition, an order parameter is simply any quantity η such that in the disordered phase $\eta = 0$ and in the ordered phase $\eta > 0$. In this case, the overall magnetisation of the sample suffices as an order parameter of the system as a function of temperature [24]. When measuring the order parameter over a range of values of T, one will find that that the net magnetisation follows

$$M \sim (T_c - T)^{\beta}, \tag{1.55}$$

where the value β is a *critical exponent* [52]. Such a value characterises the strength of the phase transition and furthermore, classifies it [53]. To clarify, any system as long as it is described by a general 2D Ising Hamiltonian, no matter the microscopic properties will exhibit a critical exponent of β when we are sufficiently within the thermodynamic limit. This phenomenon is encapsulated with the term *universality*, which is the concept that statistical models are classified by their symmetries from which a critical exponent common to all models within that symmetry class can be derived.

These concepts are similarly valid for the quantum Hall effect, as the bulk of an integer quantum Hall sample exhibits a phase transition between each of the plateaus. It is strongly believed that the transition is an Anderson-type localisation-delocalisation transition and thus has a scaling behaviour linking the correlation length ξ to a critical exponent denoted ν as [10]

$$\xi \sim |z - z_c|^{-\nu}, \tag{1.56}$$

where z is a parameter varied through the plateau transition. The correlation length ξ is a characteristic length scale over which the wavefunctions of single electrons are correlated spatially throughout the system. In the localised phase ξ must be finite

and as we move into the delocalised phase ξ becomes divergent. The rate at which the divergence occurs is quantified by ν, as expressed in equation (1.56). As with the magnetic transition, ν is believed to be characteristic of a class of phase transitions, according to universality. This means that while the critical exponent could be derived from any particular model, as long as that model is within some universality class, it ought to be the same as any other critical exponent calculated from any other models within the same universality class [54]. This is why seemingly different Hamiltonians can derive an identical critical exponent, as long as they possess the same fundamental symmetries.

Unfortunately, while the central physics of the integer quantum Hall effect is largely understood, there still remain questions surrounding the exact value of ν and a consensus on the exact value derived from theory has not been reached [9]. Immediately after the quantum Hall effect was physically realised [11], a plethora of physical theories and numerical simulations were proposed and tested [14, 55–58]. Relevant to our work, methods such as transfer matrix scaling [59], monte carlo simulation [60] and recursive Green functions [61] have been applied to models of the quantum Hall effect to derive a value of ν. From those studies, a value around $2 \leq \nu \leq 2.5$ was found. A review of the numerous approaches to this very problem is detailed in ref [9]. At the time, the numerical and theoretical predictions agreed with experimental observation, from which a value of $\nu = 2.38$ has been found [62]. With the advance of time, higher precision estimates via numerical simulation have been used to evaluate the critical exponent at $\nu = 2.593^{+0.005}_{-0.006}$ [63], drifting away from the experimental values found. Recent theoretical studies into Wess-Zumino-Witten models being used to represent the quantum Hall transition have been shown to predict a critical exponent following $\frac{1}{\nu} = 0$, i.e., the critical exponent is not well defined [64]. This is simply not consistent with the idea of universality described in the last paragraph and requires further investigation to reach a broader understanding of not only the theory of the integer quantum Hall effect, but the broader implications onto universality within physics.
This lack of consensus sufficiently motivates our ambitions in investigating plateau transitions and contributing to the discussion.

1.6.1 Renormalisation in Condensed Matter Physics

When a model exhibits a phase transition, a central goal of understanding the model naturally leads to making accurate quantifiable predictions of the phase transition. This turns into an effort to calculate the critical exponents, the values of which determine the universality class and general behaviour of that particular class of

models. Typical techniques to explore the dynamics of physical models revolve around mean-field theory [65], in which a characteristic average is taken over multiple dynamical degrees of freedom to factor out the microscopic complications and reveal the broader macroscopic phenomena. However, it is exactly the fluctuations factored out by mean-field theory which become increasingly important closer to the critical transition point [49]. A simple example of this is the Landau theory of ferromagnetism which provides a clear and intuitive depiction of the ferromagnetic transition, while failing to find the correct critical exponent for that same transition [49]. Alternatively one may seek to simulate a system of non-interacting particles directly, in the image of our quantum-mechanical treatment in section 1.2. An immediate drawback is seen as the dynamics which we seek to investigate are most prominent in the thermodynamic limit, at infinite volume. We thus seek a method which allows us to disregard computationally expensive microscopic degrees of freedom, while still taking into consideration the divergent properties of the phase transition. While many methods exist satisfying these criteria, in our work we will use a *Renormalisation Group (RG)* approach. It is 'renormalisation' as we will be renormalising as we move across length scales and it is a 'group' as the transformations form a semi-group. The difference between a group and a semi-group being the latter's lack of element inverses. Each RG element filters out degrees of freedom, removing the possibility of inverses [48]. RG methods have been utilised with great success across many branches of theoretical physics [66–69]. Here we specifically use a *Real-Space Renormalisation Group (RSRG)*, meaning a group of transformations which are coupled to the space coordinates of the model. The applicability of this procedure rests on the idea that statistical physics at phase transitions is scale invariant. In certain models, the scale invariance extends to conformal invariance, a much stricter symmetry class which allows for the study via conformal field theory [70]. Before introducing our implementation of the RG, we provide a historical example of Kadanoff's block spin approach [71] to clarify the ideas behind the RG, specifically in real space.

1.6.2 Kadanoff's Block Spin Approach

We start with a simple 2D Ising spin model on a square lattice consisting of sites with spin S_i, with the index notating the site. Nearest neighbour spins interact with one another leading to a Hamiltonian H which takes the form

$$\beta_T \mathcal{H} = -K \sum_{\langle ij \rangle} S_i S_j - h \sum_i S_i, \tag{1.57}$$

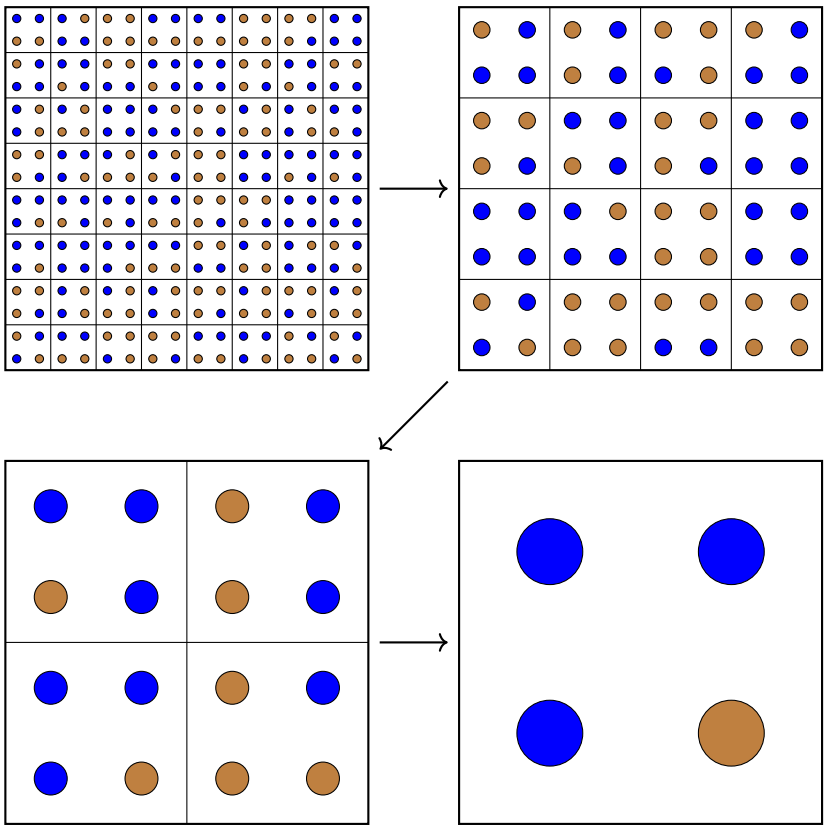

Figure 1.4: Multiple steps of a block spin renormalisation transformation. Dots represent individual spins, coloured either blue or brown. In the top left spins are grouped into 2×2 clusters and an average over this cell determines the colour of the transformed system. Consecutive iterations are shown by following the arrows, starting in the top left and ending in the bottom right. Each transformation doubles the characteristic length scale and halves the correlation length for the new Hamiltonian. Smaller length scales are progressively filtered out in real space to facilitate the determination of scaling properties.

with $\beta_T = \frac{1}{k_B T}$, h represents an applied magnetic field interacting with individual spin sites, and K denotes the strength of nearest neighbour interaction. The sum index $\langle ij \rangle$ is a shorthand for a sum over nearest neighbour sites i and j only. Due to the nearest-neighbour interactions, spins are correlated to some length dependent on temperature $\xi(T)$. If we are close enough to the critical point, where correlation length diverges, then low multiples of the lattice spacing fall well below this correlation length, and hence we assume that clusters of spins on this length scale can be treated as a singular unit [49]. We directly exploit our assumption by taking a $l \times l$ block such that if we denote the lattice spacing a, then $la \ll \xi(T)$. Using these blocks, we wish to reformulate the Hamiltonian treating the blocks as the original

(1.57) treats individual spin sites. Our central assumption here is that in doing so, the $l \times l$ blocks interact with other blocks just as individual spins interact with one another. Doing so we can define the block spin S_I which describes the average spin over the constituents of that block.

$$S_I = \frac{1}{4|m_s|} \sum_{i \in I} S_i. \tag{1.58}$$

In this equation, m_s denotes the average magnetisation over the block,

$$m_s = \frac{1}{4} \sum_{i \in I} \langle S_i \rangle. \tag{1.59}$$

Our assumption brings us to a similar Hamiltonian for the system of 2×2 blocks, namely

$$\beta_T \mathcal{H}_l = K_l \sum_{\langle IJ \rangle}^{N/l^2} S_I S_J + h_l \sum_{I}^{N/l^2} S_I. \tag{1.60}$$

The transformation from sites to blocks, to blocks of blocks etc. is depicted in 1.4 for a 2×2 block transformation. In performing this reformulation of the Hamiltonian, the absolute correlation length $\xi(T)$ remains unchanged, while the new Hamiltonian is defined on a length scale twice that of the original Hamiltonian. This results in the effective correlation length of the new Hamiltonian being $\frac{1}{l}$ that of the original. This signifies a Hamiltonian further from criticality and thus compared to the original reduced temperature $\tau = \frac{T - T_c}{T_c}$, the new Hamiltonian obtains a new reduced temperature τ_l. If we consider the free energy per spin of the system $f_s(\tau, h)$, the fact that the block Hamiltonian is of the same form as the original with different parameters allows for the relation

$$f_s(\tau_l, h_l) = l^2 f_s(\tau, h). \tag{1.61}$$

To deduce the critical properties of this model we assume that the parameters of the block Hamiltonian take the form

$$\tau_l = \tau l^{\lambda_\tau}, \tag{1.62a}$$

$$h_l = h l^{\lambda_h}, \tag{1.62b}$$

and we additionally assume both λ_τ and λ_h to be positive. This is a fairly strong assumption and in Kadanoff's original work, a clear justification of these assumptions had not been found. Shortly after in a series of papers by Wilson [69], the

conditions under which these assumptions are valid were expounded and clarified. Once substituted into (1.61) our assumptions lead us to an alternate expression of the free energy as

$$f_s(\tau, h) = \frac{1}{l^2} f_s(\tau l^{\lambda_\tau}, h l^{\lambda_h}). \tag{1.63}$$

Now we are free to choose a value of l such that $l^{\lambda_\tau}|\tau| = 1$. Taking this into account, we can rewrite equation (1.63) as

$$f_s(\tau, h) = |\tau|^{\frac{2}{\lambda_\tau}} f_s\left(1, \frac{h}{|\tau|^{\frac{\lambda_h}{\lambda_\tau}}}\right). \tag{1.64}$$

We have successfully derived a scaling relation for the free energy density, in terms of a single parameter functional taking the form of the original Hamiltonian, and a scaling factor defined in terms of exponents; critical exponents. This brief derivation shows us the power behind a selective reduction of degrees of freedom, specifically in terms of spatial coordinates across multiple length scales. This is the focal idea behind the RG and a similar derivation is used in section 2.2.3 to determine a value of ν.

Chapter 2

The Chalker-Coddington Model and Real-Space Renormalisation

2.1 Introduction to the Model

While previously we have rather rapidly produced a working model describing the plateaux of the quantum Hall effect, our models tell us nothing about the transition between the plateaux and more specifically the critical point. We thus turn to a different model, which can more accurately predict the physics of this transition. As we are only interested in the behaviour of the system as a whole at the transition point, we forgo the desire for a truly microscopic model and turn to a model which focuses solely on the transition phenomena and the critical properties thereof. As is seen from the experimental data, the bulk of the quantum Hall sample is insulating at plateaux. Additionally, while transitioning from plateau to plateau, a quantum Hall sample will briefly exhibit non-zero longitudinal resistivity as seen in figure 1.2 [11]. We thus want a model which undergoes a localisation-delocalisation-localisation transition.

Shortly after the experimental realisation of the quantum hall effect, such a model was introduced by Chalker and Coddington which describes the motion of non-interacting electrons along a disordered potential in the form of a network [58]. The *Chalker-Coddington network model* neatly links ideas from percolation theory and Anderson localisation to the quantum Hall effect. The model consists of nodes which signify saddle points in a disordered, slowly varying 2D potential, and links between nodes which signify equipotentials between *saddle points*. The 2D potential manifests the weak disorder discussed in section 1.2.2 which evokes the bulk localisation characteristic of the quantum Hall effect. The electrons are bound to these

equipotentials until they approach the neighbourhood of a saddle point. In this situation, there exists a probability amplitude associated with the electrons quantum tunnelling through the potential barrier imposed by the saddle point. Naturally, there is a reciprocal probability amplitude with the electron simply continuing along its present equipotential. From the perspective of an electron travelling along an equipotential at one side of the sample, with successive transmissions past saddle points, it may pass through and reach the other side of the sample. When an electron exhibits traversal across the entire network, it is said to percolate, with the overall phenomenon referred to as *percolation*. When the heights of the saddle points are modified within the potential landscape, particularly when the heights are brought close to the electron potential (set uniformly to 0 without loss of generality), the probability amplitude of tunnelling increases. The relationship between probability amplitude and saddle point height is not linear and will be explored further later in the chapter. When the saddle point heights of the entire system are altered, one can see how this affects the localisation of the electrons within the system. At a particular distribution(which must be centred at 0) of saddle point heights, the electrons can percolate throughout the entire lattice. At the percolating limit, the electrons are delocalised and the distribution representing the electrons is referred to as the critical *Fixed Point (FP) distribution*. In general, an FP distribution represents a configuration of the model which is scale invariant [52]. Due to the landscape being constructed from saddle points, which can be both raised and lowered to inhibit quantum tunnelling, there is not one localised phase, but two, separated by the critical FP distribution. We can clearly link the behaviour of the model described to the physics of the plateau to plateau transition in the quantum Hall regime, where the bulk exhibits delocalised behaviour at criticality, but localised behaviour at the higher and lower plateaux between which the critical point resides.

To describe our previous discussion more explicitly, we can take the assumption of a regular square lattice on which the saddle points and equipotentials sit. Each node is thus equipped with 4 connecting edges, which form the incoming and outgoing equipotentials on either side of the saddle point. A linear combination of incoming electrons wavefunctions will form the wavefunctions of outgoing electrons. This is simply because the outgoing magnitude on either side will be composed of the reflected electrons on the same equipotential together with the tunnelled electrons from the opposing equipotential. Thus, the saddle point can be described as a matrix relating the incoming electrons to the outgoing electrons. This will be a 2×2 square matrix, and from considering charge conservation, the matrix must be unitary such that the overall magnitude of the incoming wavefunction does not change.

We thus seek the most general $U(2)$ matrix. To derive our sought after matrix we begin with the most general 2×2 matrix

$$U = \begin{bmatrix} a & b \\ c & d \end{bmatrix}. \tag{2.1}$$

From which we know that $UU^\dagger = I$ and that $UU^{-1} = I$ via the unitary condition. This implies that $U^\dagger = U^{-1}$, i.e.,

$$\begin{bmatrix} a^* & c^* \\ b^* & d^* \end{bmatrix} = \frac{1}{\det U} \begin{bmatrix} d & -b \\ -c & a \end{bmatrix}. \tag{2.2}$$

We can read off from this that $d^* \det U = a$ and $a^* \det U = d$, which means that $|\det U|^2 a = a$. This implies that either $a = 0$ or

$$\det U = ad - bc = e^{i\phi}. \tag{2.3}$$

We can take this condition to find $d = a^* e^{i\phi}$ and $c = -b^* e^{i\phi}$ such that the original matrix is

$$U = \begin{bmatrix} a & b \\ -e^{i\phi} b^* & e^{i\phi} a^* \end{bmatrix}. \tag{2.4}$$

When we take the determinant we find the additional restriction $|a|^2 + |b|^2 = 1$. As desired, equation (2.4) defines the most general 2×2 unitary matrix from which we can describe the nodes in the Chalker-Coddington model.

To link our matrix to the Chalker-Coddington model we relate the incoming and outgoing electrons from a saddle point with

$$\begin{bmatrix} I \\ I* \end{bmatrix} \begin{bmatrix} a & b \\ -e^{i\phi} b^* & e^{i\phi} a^* \end{bmatrix} = \begin{bmatrix} O \\ O* \end{bmatrix}, \tag{2.5}$$

where I, $I*$ represent incoming electron channels and O, $O*$ represent outgoing electron channels. Without loss of unitarity we can set $\phi = \pi$ such that

$$U = \begin{bmatrix} a & b \\ b^* & -a^* \end{bmatrix}. \tag{2.6}$$

Finally, we rename our variables a and b as they represent the probability amplitudes of transmission and reflection. We thus write

$$U = \begin{bmatrix} t & r \\ r & -t \end{bmatrix}, \tag{2.7}$$

where from our model we take the probability amplitudes to be real, since $|t|^2+|r|^2 = 1$ is still satisfied. A node represented by this matrix is depicted in figure 2.3. As previously pointed out, for any saddle point there is a direct link between the transmission amplitude t and the saddle point height, which we denote z. It has been shown [72] that the transmission probability, which is directly related to the conductance $g = |t|^2$ in a quadratic saddle point is related to z as

$$g = \frac{1}{1 + e^z}. \tag{2.8}$$

In our particular method, the distribution of z will be important in both calculating the critical exponent and relating the numerical results to the physical model. From individual nodes, we can construct the model by tiling the nodes in a 2D square lattice such that the directed edges line up as shown in figure 2.1. While the figure shows a segment of an infinite sample, the Chalker-Coddington model still achieves accurate results in the finite regime. If a finite system is constructed, there necessarily exists a boundary, for which nodes along the edge will not have endpoints for two of the node's edges. In this case, the 'loose' edges are directed into the following node along the boundary. Our decision to do so allows for a more accurate depiction of the quantum Hall effect, particularly in the demonstration of edge states. To see this we increase the saddle point heights z of each node, so every node exists with $t = 1, r = 0$. Such a scenario is depicted in figure 2.2. The figure shows an entirely localised bulk, but transport via an equipotential around the very edge of the sample. A similar scenario occurs upon lowering, instead of raising, the saddle point heights. These two extremes exhibit the two bulk localised phases of the upper and lower plateaux. It follows that between these extremes, for a particular distribution of saddle point heights, there exists a system which is not localised in the bulk. The next section develops the tools needed to find this distribution.

2.2 Real-Space Renormalisation Approach

In applying an RSRG approach in a very physical and analytical way to the plateaus transition, we can demonstrate the localisation transition and find the critical expo-

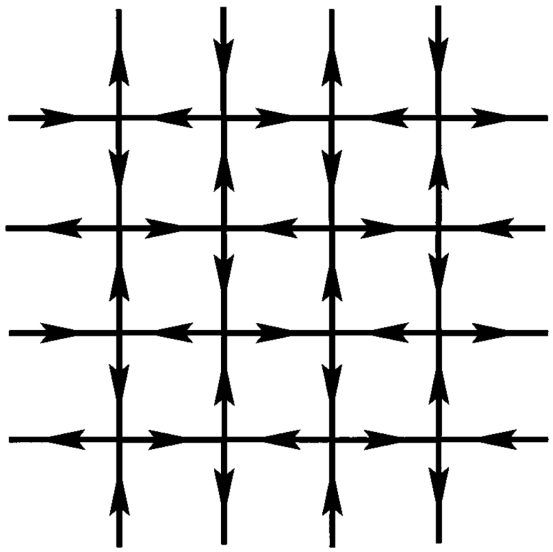

Figure 2.1: A 2D lattice consisting of Chalker-Coddington type nodes. Directly neighbouring nodes are rotated by $\frac{\pi}{2}$ such that the directed edges are consistent. Taken From [73].

nent. As an overall outline of how we apply the RSRG to the Chalker-Coddington model, we start by finding a renormalisation transformation which amplifies the length scale of the system, much like Kadanoff's procedure in section 1.6.2. Upon finding the transformation, we will repeatedly apply the transformation to the system while keeping the distribution of z values symmetric and centred upon 0, in order to determine the FP distribution at criticality. Once we have ascertained that the system is in criticality, we repeatedly apply the transformation once more, moving the system out of criticality as described in section 1.6.2. As the system moves out of criticality, we can directly measure the strength of the diverging correlation length, which allows for numerical approximation of the critical exponent, as will be derived in section 2.2.3.

2.2.1 Deriving the Renormalisation Transformation

To begin deriving the renormalisation transformation we start by constructing a unit cell from our previously discussed scattering nodes. The only restriction on the creation of a unit cell is that it possesses the same number of connecting edges as the individual nodes and that it resembles the structure of the underlying lattice being investigated. This allows for an iterative 'coarse graining' procedure which effectively builds a large system size, without incurring the extensive computational

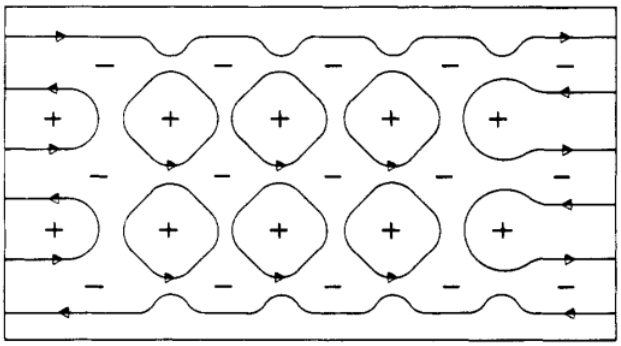

Figure 2.2: A rectangular finite size sample of the Chalker-Coddington model. All saddle point heights are taken to the extreme positive limit such that all equipotentials in the bulk form small loops, while a single equipotential spans the edge, facilitating conduction. It represents the quantum Hall system in a conductivity plateau. Taken from [58].

burden of simulating each individual lattice site. The enlarging effect of this procedure on this model also allows us to analyse the scaling behaviour, i.e. the critical exponent, in a straightforward manner. Previously multiple different unit cells have been constructed on the square lattice, of which the unit cell consisting of 5 nodes has been shown to most accurately reproduce the physics at the transition [74]. This unit cell is shown in figure 2.4

The renormalisation procedure consists of finding a matrix S' of the same form as the individual S which describes the scattering properties of the entire unit cell. To this end, we endeavour to explicitly write out the linear equations governing the inputs and outputs of each node within the unit cell. One singular node and its connecting nodes can thus be described

$$S \begin{bmatrix} I \\ I* \end{bmatrix} = \begin{bmatrix} t & r \\ r & -t \end{bmatrix} \begin{bmatrix} I \\ I^* \end{bmatrix} = \begin{bmatrix} O \\ O^* \end{bmatrix}. \tag{2.9}$$

In this equation we are neglecting the phase accrued across equipotentials, these are explicitly included in the following calculations.
We then use the connections between nodes to eliminate extraneous variables within the equations and we find the following relation pertaining to the inputs and outputs of all nodes within the unit cell,

$$\mathbf{A}x = b, \tag{2.10}$$

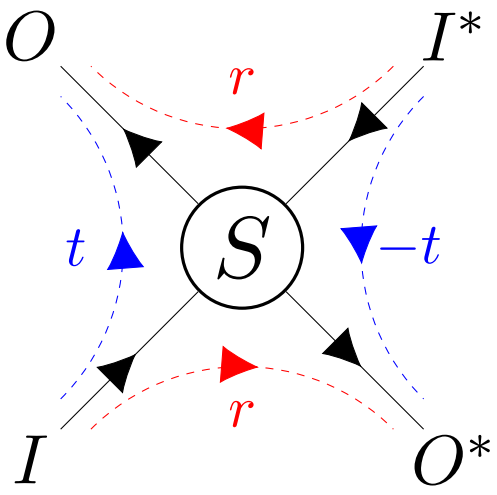

Figure 2.3: Diagram of a single saddle point represented by the node S. Edges adjoining S are directed according to arrows. Each edge is labelled O, I^*, O^*, I with respect to the node. Dashed arrows represent possible trajectories across the saddle point, with accompanying labels describing the probability amplitude of that trajectory. Dashed arrows are coloured depending on whether they represent transmission (blue), or reflection (red).

with

$$A = \begin{bmatrix} 1 & 0 & 0 & 0 & 0 & -r_1 e^{i\phi_{31}} & 0 & 0 & 0 & 0 \\ 0 & 1 & 0 & 0 & 0 & t_1 e^{i\phi_{31}} & 0 & 0 & 0 & 0 \\ 0 & -t_2 e^{i\phi_{12}} & 1 & 0 & 0 & 0 & 0 & -r_2 e^{i\phi_{42}} & 0 & 0 \\ 0 & -r_2 e^{i\phi_{12}} & 0 & 1 & 0 & 0 & 0 & t_2 e^{i\phi_{42}} & 0 & 0 \\ 0 & 0 & -r_3 e^{i\phi_{23}} & 0 & 1 & 0 & 0 & 0 & 0 & -t_3 e^{i\phi_{53}} \\ 0 & 0 & t_3 e^{i\phi_{23}} & 0 & 0 & 1 & 0 & 0 & 0 & -r_3 e^{i\phi_{53}} \\ 0 & 0 & 0 & 0 & t_4 e^{i\phi_{34}} & 0 & 1 & 0 & 0 & 0 \\ 0 & 0 & 0 & 0 & -r_4 e^{i\phi_{34}} & 0 & 0 & 1 & 0 & 0 \\ -t_5 e^{i\phi_{15}} & 0 & 0 & 0 & 0 & 0 & -r_5 e^{i\phi_{45}} & 0 & 1 & 0 \\ -r_5 e^{i\phi_{15}} & 0 & 0 & 0 & 0 & 0 & t_5 e^{i\phi_{45}} & 0 & 0 & 1 \end{bmatrix} \tag{2.11a}$$

$$x = \left[O_1, O_1^*, O_2, O_2^*, O_3, O_3^*, O_4, O_4^*, O_5, O_5^*\right]^T \tag{2.11b}$$

$$b = \left[t_1 I_1, r_1 I_1, 0, 0, 0, 0, r_4 I_4^*, t_4 I_4^*, 0, 0\right]^T. \tag{2.11c}$$

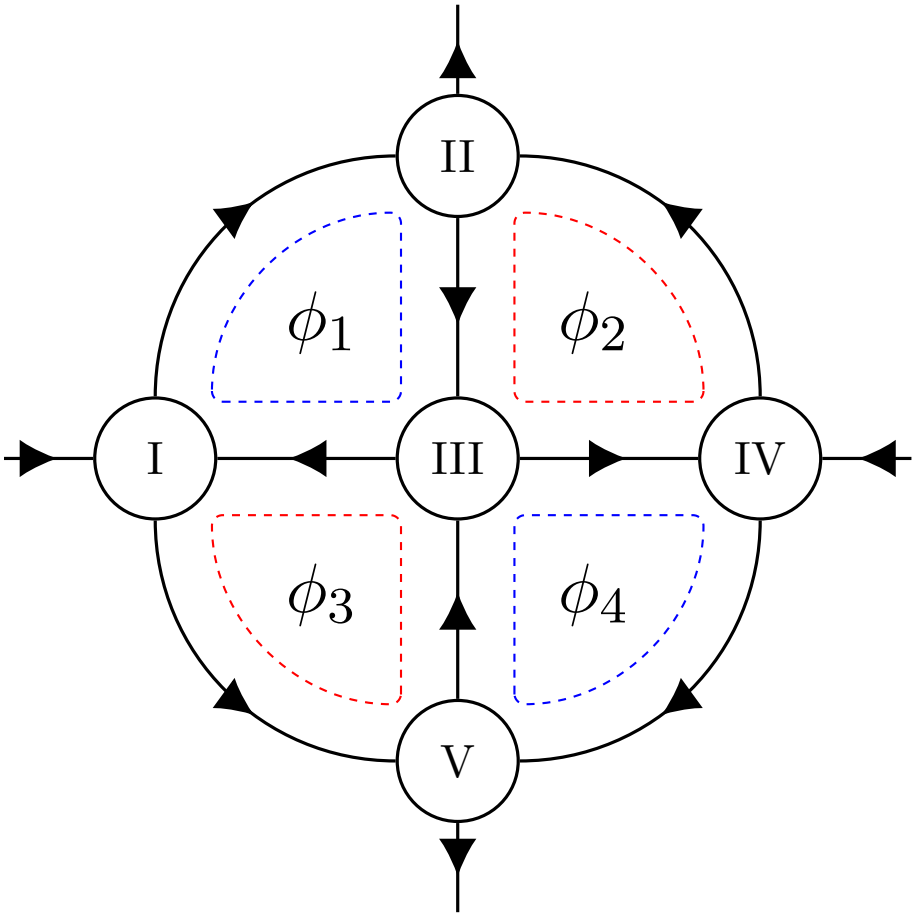

Figure 2.4: An *RSRG unit cell.* Consisting of 5 saddle points, it is the smallest such construction which satisfies self-similarity with respect to edges. Nodes within the unit cell are labelled with Roman numerals. Phases exist along each edge of the network, although in calculations these simplify to the four phases $\phi_1, \phi_2, \phi_3, \phi_4$ representing the phase accumulated upon traversing the edges associated with the dashed loop surrounding the label.

In this expression $e^{i\phi_{\alpha\beta}}$ refers to the phase accrued across the edge going from node indexed α to node indexed β. Each parameter is indexed with reference to the node it belongs to within the unit cell, as are the inputs and outputs. We can invert this matrix and after some algebra, we find a *renormalised t' coefficient* as

$$t' = \left| \frac{\begin{array}{r} -e^{i(\phi_1+\phi_4-\phi_2)} r_1 r_3 r_5 t_2 t_4 + e^{i(\phi_1+\phi_4)} t_2 t_4 \\ - e^{i\phi_4} t_1 t_3 t_4 + e^{i\phi_3} r_2 r_3 r_4 t_1 t_5 - e^{i\phi_1} t_2 t_3 t_5 \end{array}}{\begin{array}{r} -1 - e^{i\phi_3} r_2 r_3 r_4 + e^{i\phi_2} r_1 r_3 r_5 + e^{i(\phi_2+\phi_3)} r_1 r_2 r_4 r_5 \\ + e^{i\phi_1} t_1 t_2 t_3 - e^{i(\phi_1+\phi_4)} t_1 t_2 t_4 t_5 + e^{i\phi_4} t_3 t_4 t_5 \end{array}} \right|. \tag{2.12}$$

This renormalised coefficient represents the transmission amplitude of the entire

unit cell, i.e., the probability amplitude that the equipotential inbound at node I_1 leaves via node O_2.

There is a slight caveat to this derivation. When we formed the unit cell, the outermost four saddle points within the cell all lie in the same orientation while the central saddle point lies in a different orientation. Furthermore, there are two distinct ways to place the central saddle point, either rotated 90° clockwise from the outer saddle points, or 90° anti-clockwise. What we have derived so far stems from a clockwise rotation of the central saddle point. But to show consistency within the model, we have also derived the renormalisation transformation from a counter-clockwise rotated central saddle point. The connections between the nodes are altered slightly by this different geometry. The result is a modified expression for the renormalised t',

$$t' = \left| \frac{\begin{array}{r} -t_1t_5 + e^{i(\phi_1+\phi_4-\phi_2)}r_1r_3r_5t_2t_4 + -e^{i(\phi_1+\phi_4)}t_2t_4 \\ - e^{i\phi_4}t_1t_3t_4 - e^{i\phi_3}r_2r_3r_4t_1t_5 + e^{i\phi_1}t_2t_3t_5 \end{array}}{\begin{array}{r} -1 - e^{i\phi_3}r_2r_3r_4 + e^{i\phi_2}r_1r_3r_5 + e^{i(\phi_2+\phi_3)}r_1r_2r_4r_5 \\ + e^{i\phi_1}t_1t_2t_3 - e^{i(\phi_1+\phi_4)}t_1t_2t_4t_5 + e^{i\phi_4}t_3t_4t_5 \end{array}} \right|. \tag{2.13}$$

As is shown in 2.5, the two transformations have identical outcomes along the range of t. We will use equation (2.12) henceforth.

2.2.2 Determination of the Critical Fixed Point Distribution

To implement the RG transformation, first an initial distribution of coefficients must be created artificially. Subsequently, the transformation is applied to this distribution from which a new distribution of renormalised coefficients is generated. The initial distribution of t values, $P(t)$ used is made so that t^2 is symmetric about 0.5. We start with this particular distribution as it lies closer to the critical FP distribution - which we seek to determine - than the trivial FP distributions. Different starting distributions, such as a $P(t)$ with t symmetric about 0.5, have been implemented to more limited success [74]. Each subsequent $P(t)$ of renormalised coefficients is generated from the last via equation (2.12). Unless otherwise stated, in this project we used 10^9 coefficients to generate the succeeding distribution. This amount of coefficients is an improvement upon previous studies [74], and can result in a more robust numerical approximation of ν, as will be discussed later. After successive applications of the renormalisation procedure, the distribution of coefficients begins to converge upon an FP distribution. Within the Chalker-Coddington model, there are three FP distributions, 2 trivial fixed points located around $t = 1$ and $t = 0$, and another for which the distribution in terms of z is centred around

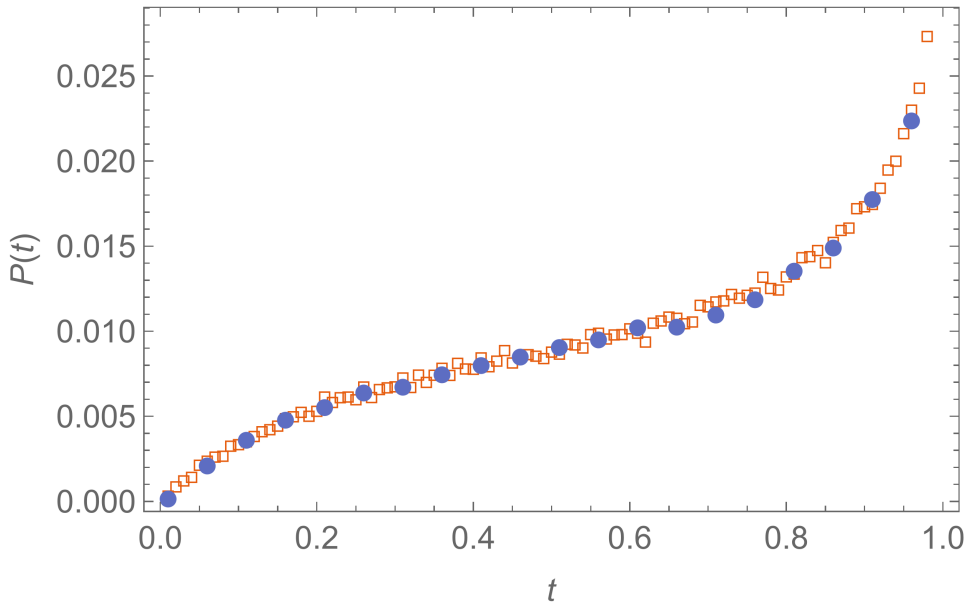

Figure 2.5: The $P(t)$ distributions after four renormalisation steps for 100000 samples. Orange squares signify the $P(t)$ distribution under the transformation defined in equation (2.12) and blue circles signify the $P(t)$ distribution under the alternate transformation defined in equation (2.13). For the latter, only every 5th data point is shown for visual clarity.

0. In terms of t, it refers to the value of $t = \frac{1}{2}$. The latter distribution is the distribution of fixed points at criticality, in the percolating limit. As the renormalisation transformation would typically push the system further out of criticality, to avoid the convergence to the trivial fixed points $t = 1$ and $t = 0$, we symmetrise the distribution of z values, henceforth $Q(z)$, around 0 after every renormalisation step. The resulting $Q(z)$ is approximately Gaussian. The effect of successive application of our described procedure upon $P(t)$, the conductance distribution $G(g)$ and $Q(z)$ is shown in figs. 2.6 to 2.8. After starting with an artificial $P(t)$ which is linear in t, the distribution can be seen to rapidly converge to the FP distribution.

2.2.3 Critical Exponent obtained from the Model

Now we have numerically converged upon a distribution of saddle point heights which represents the system in criticality. To investigate the properties of the model at criticality, we shift the entire $Q(z)$ distribution out of criticality by a predetermined value, z_0, after which the RG transformation is again repeatedly applied to the distribution without symmetrising. An exaggerated representation of this

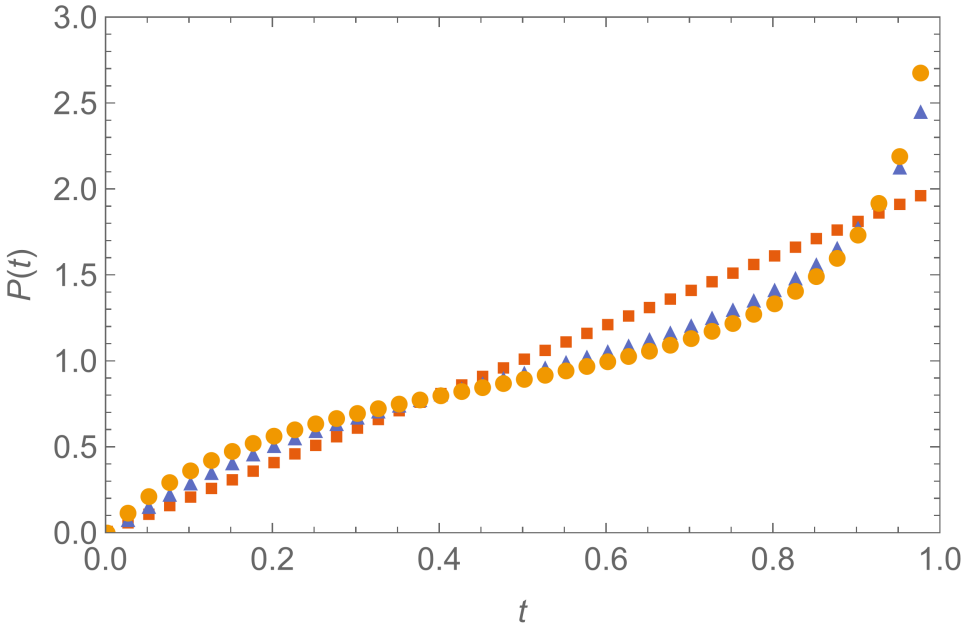

Figure 2.6: The $P(t)$ distribution after multiple renormalisation steps. Red squares signify the initial fabricated distribution, blue triangles signify $P(t)$ after a single renormalisation step and orange circles signify $P(t)$ after 12 renormalisation steps.

procedure is shown in figure 2.9, while data used for the calculation of ν in this thesis is shown in figure 2.10. As the distribution naturally drifts away from the FP distribution and towards the trivial fixed point, critical properties can be deduced from the rate at which the FP distribution shifts away from its original point. Such an analysis is called an *RG flow*. In particular, as z can be directly linked to the correlation length, the maxima of successive $Q(z)$ distributions will be used in the following section to directly calculate the critical exponent ν. Due to numerical fluctuations commonly occurring in the calculation of $Q(z)$ distributions, it is important not to take the largest value from the distribution as the maximum, as it may not represent the most accurate maximum for that distribution. Instead, to ensure higher accuracy, we assume a Gaussian form to the tip of the z distribution. By fitting a Gaussian curve to the top 5% of the $Q(z)$ distribution, the value found for the mean serves as an accurate estimate for the maximum. To further improve numerical stability in the calculated maximum, we split the dataset into 10 smaller subsets, and estimate the maxima of each via the outlined Gaussian approximation. The arithmetic mean is taken of the 10 maxima, thereby landing upon the value for $Q(z)$ maxima which we will henceforth use in determining ν.

When a renormalisation transformation is applied to the model, the physical

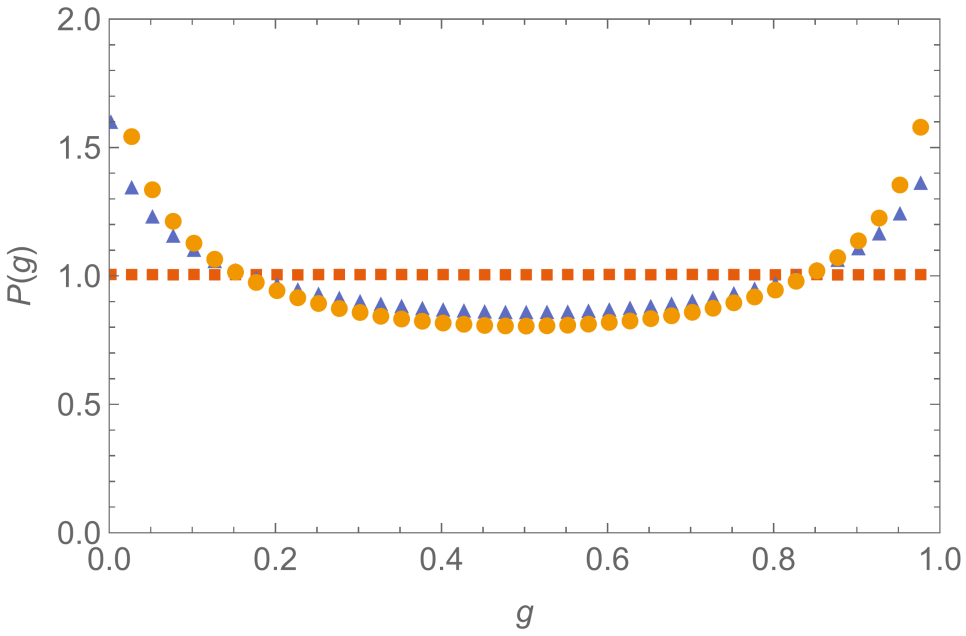

Figure 2.7: The $P(g) = P(t^2)$ distribution after multiple renormalisation steps. Similarly to figure 2.6, red squares signify the initial distribution, blue triangles signify $P(g)$ after a single renormalisation step and orange circles signify $P(g)$ after 12 renormalisation steps.

value of the correlation length does not change. However, as mentioned previously in section 1.6.2, at each iteration our length scale changes along with the renormalisation transformation. In our case, the renormalisation transformation the 'length' of a single node is two edges, whereas the 'length' of a renormalised unit cell is four edges. We therefore scale the system by a factor of 2 and so our effective correlation length changes according to

$$\xi' = \frac{\xi}{2}. \tag{2.14}$$

In terms of the initial distribution shift value z_0 and each subsequent maxima of the $Q(z)$ distribution, z_n, we can thus define the relation

$$\xi(z_n) = \frac{\xi(z_0)}{2^n}. \tag{2.15}$$

In contrast, the maxima of the saddle point height distribution scales with an unknown quantity. It is the comparison of these two scaling factors which will result in the critical exponent for the correlation length. For small values of initial bias $z_0 \ll 1$ The resulting maxima z_n have an approximately linear relationship to the original z_0 value. Thus the maxima of consecutive RG flow distributions is linked

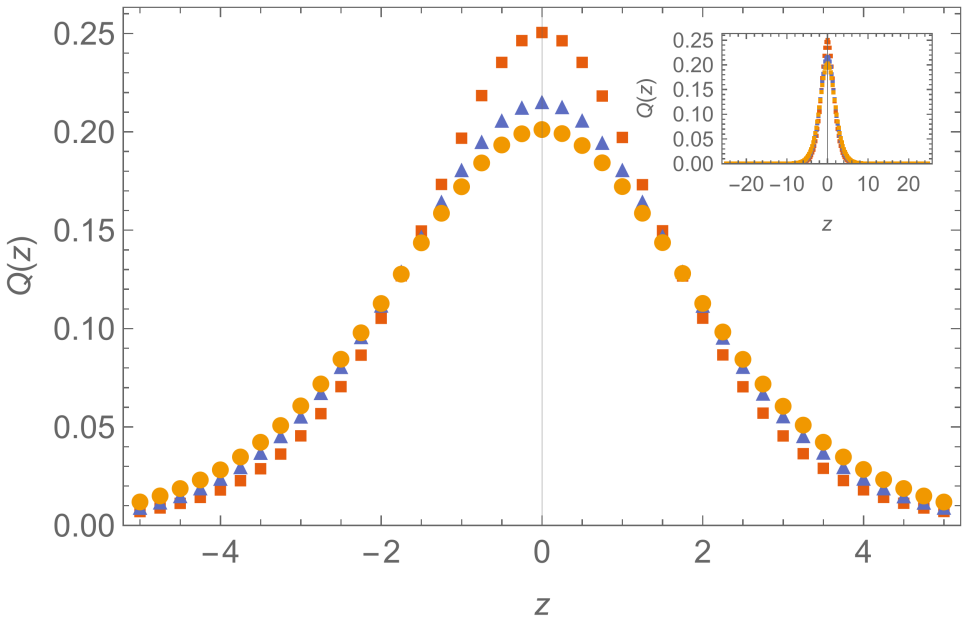

Figure 2.8: The $Q(z)$ distribution after multiple RG steps. The main figure shows the distribution for $-5 \leq z \leq 5$ for visual clarity with the inset plot showing the distributions for the entire range of z. Similarly to figure 2.6, red squares signify the initial distribution, blue triangles signify $Q(z)$ after a single renormalisation step and orange circles signify $Q(z)$ after 12 renormalisation steps.

to z_0 as

$$z_n = (2^{\varepsilon})^n z_0. \tag{2.16}$$

In this relation, ε is a variable determined by the data. Consequently, whatever we exponentiate with ε can be chosen freely, we choose 2^{ε} as it reminds us of the real-space scaling factor we are working with throughout the derivation. Our choice will also allow for simplifications in the final expression used for calculating ν.
It follows from the behaviour of ξ that

$$\xi(z_0) = 2^n \xi([2^{\varepsilon}]^n z_0) = 2^n \xi([2^n]^{\varepsilon} z_0). \tag{2.17}$$

We then identify $2^n = \left(\frac{z_n}{z_0}\right)^{\frac{1}{\varepsilon}}$ such that

$$\xi(z) = \left(\frac{z_n}{z_0}\right)^{\varepsilon} \xi\left\{\left[\left(\frac{z_n}{z_0}\right)^{\varepsilon}\right]^{\frac{1}{\varepsilon}} z_0\right\} = \left(\frac{z_n}{z_0}\right)^{\varepsilon} \xi(z_n). \tag{2.18}$$

Now here we need that $\xi(z_n) \sim 1$ which requires us to apply the renormalisation transformation enough times such that we are far away from criticality. With this

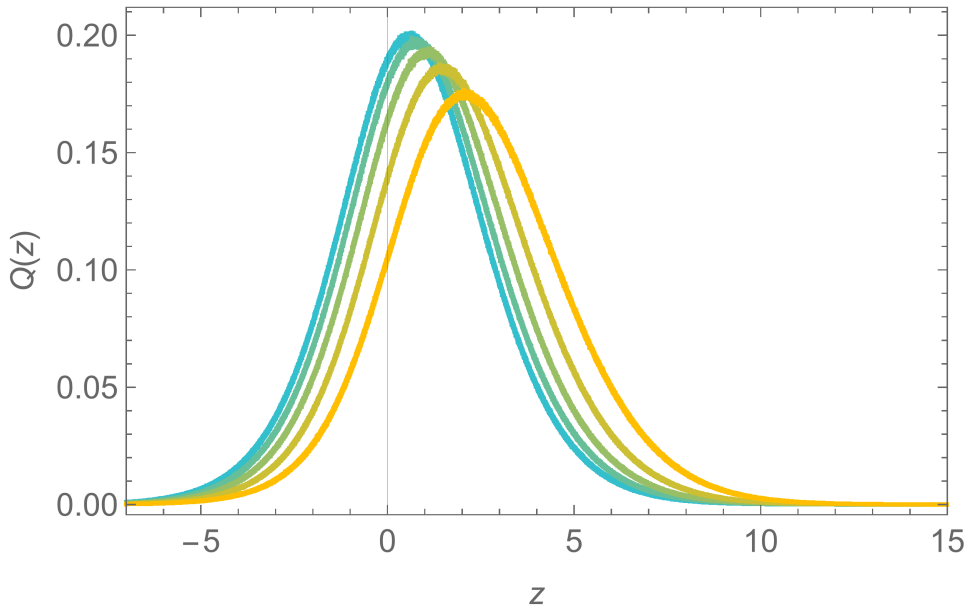

Figure 2.9: For $z_0 = 0.5$, four successive $Q(z)$ distributions after each application of the renormalisation transformation are shown. While in our determination of ν, we use much smaller z_0 values, this plot demonstrates how the distribution shifts away from the FP distribution (centred on $z = 0$) and towards the trivial fixed points.

satisfied we have

$$\xi \sim z_0^{-\varepsilon}, \tag{2.19}$$

which will make it clear now that ε is the critical exponent ν that we are looking for. To find the value for ν we return to our earlier equation

$$2^n = \left(\frac{z_n}{z_0}\right)^{\nu}, \tag{2.20}$$

and joyfully rearrange to find

$$\nu = \frac{\ln 2^n}{\ln\left(\frac{z_n}{z_0}\right)}. \tag{2.21}$$

This is the equation we shall use to calculate the critical exponent, given large enough n. In implementation, what this means is we numerically calculate the z_n for multiple values of z_0. After doing so we fit a line to the resulting data for each RG step as shown in figure 2.11. The gradient of this line is what we use for the value $\frac{z_n}{z_0}$ in equation (2.21).

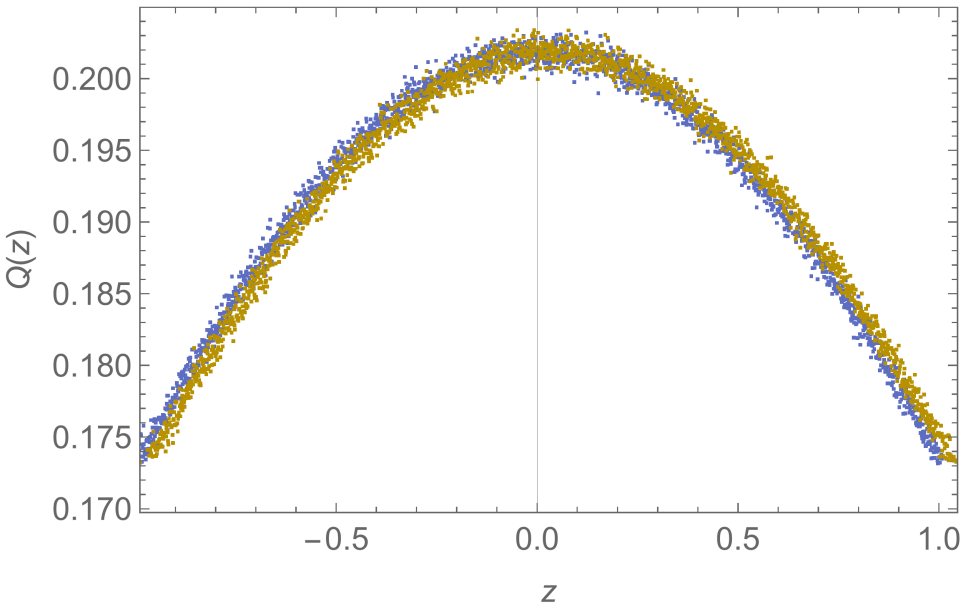

Figure 2.10: For $z_0 = 0.007$,The FP $Q(z)$ distribution in blue is compared with the distribution after 7 renormalisation steps, in brown. Both distributions are averaged over 10 separate instances of the entire procedure. Only values $-1 \leq z \leq 1$ are shown for visual clarity.

2.3 Stability of the Fixed Point Distribution

Naturally, when undertaking any numerical work the primary goal is to ensure any results are as precise as is feasibly possible. In this section, we review our methodology in order to achieve this. In previous literature, 10^7 scattering matrix coefficients were used to calculate successive renormalisation steps [75]. To improve upon this, in our work we use 10^9 coefficients in our calculation of the quantum Hall critical exponent. In later sections, this is lowered to 10^8 due to the additional parameters being concurrently studied. To make sure we were using the most accurate representation of the FP distribution, we iterated the RG procedure until fluctuations of the mean-square deviation $\Delta_n = \frac{1}{N}\int \sqrt{Q_{n+1}(z)^2 - Q_n(z)^2}$ between iterations fell below 10^{-3}. Figure 2.12 displays our results showing the rapid convergence as Δ approaches 0. We also show that the standard deviation of the resulting FP distribution converges to 2.171. The standard deviation σ_z as a function of RG step is shown in figure 2.13 and the derivative $\sigma_z' = \frac{\mathrm{d}\sigma_z}{\mathrm{dstep}}$ at those points (based on splines interpolating the points) is shown in figure 2.14. The FP distribution was evaluated a total of 10 times. Our results on the FP distribution are consistent with what was previously found.

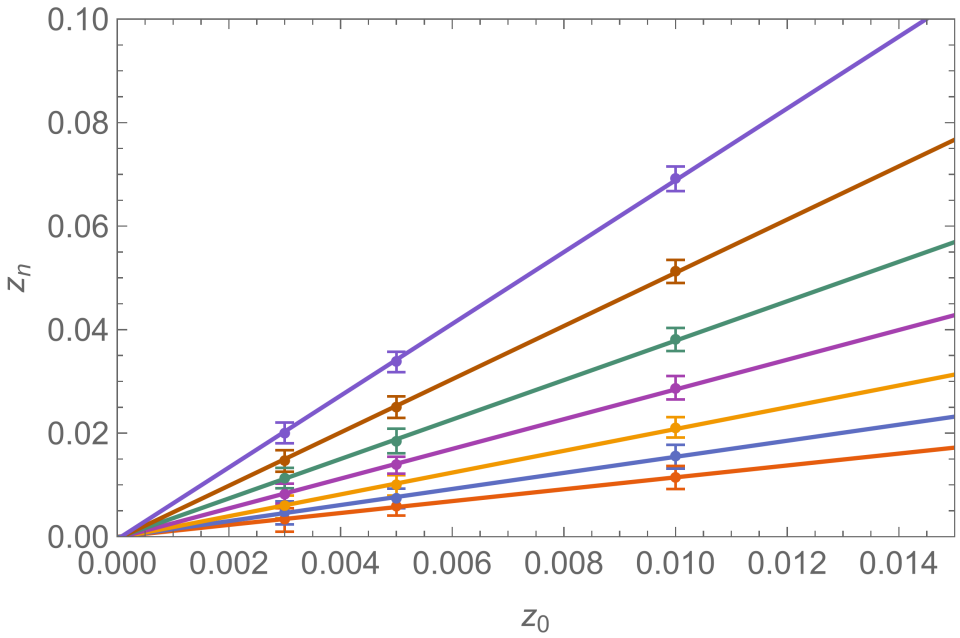

Figure 2.11: A plot of initial z_0 values compared with the maxima value z_n after each consecutive RG step away from the FP distribution. Each RG step increases the gradient of the plotted rays and is represented by a different colour. What is shown is an average over 10 instances of the renormalisation procedure, to limit the amount of data points shown.

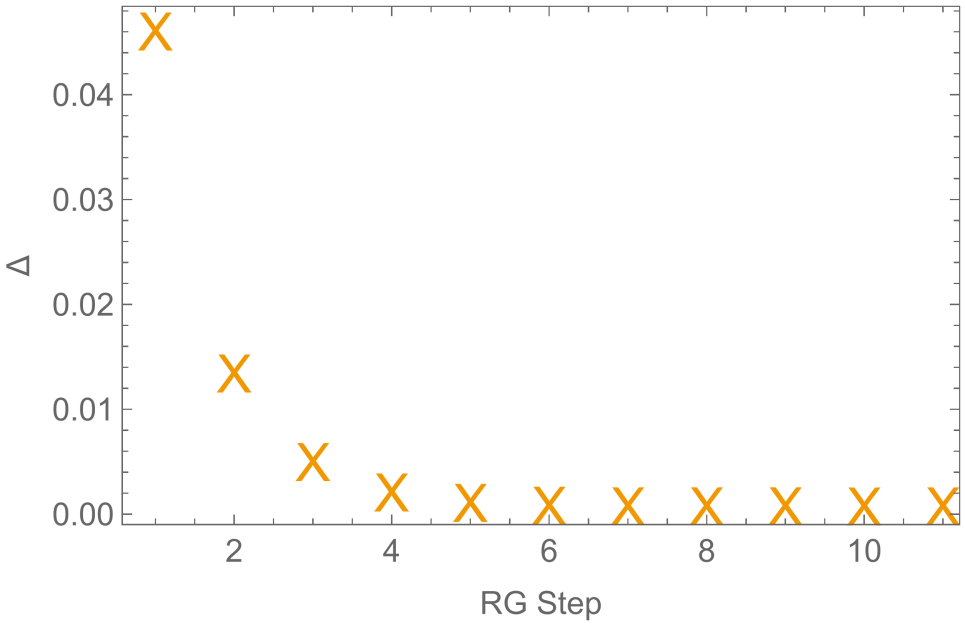

Figure 2.12: Mean square deviation ($\Delta_n = \frac{1}{N}\int \sqrt{Q_{n+1}(z)^2 - Q_n(z)^2}$) of successive $Q(z)$ distributions upon repeated application of the renormalisation transformation.

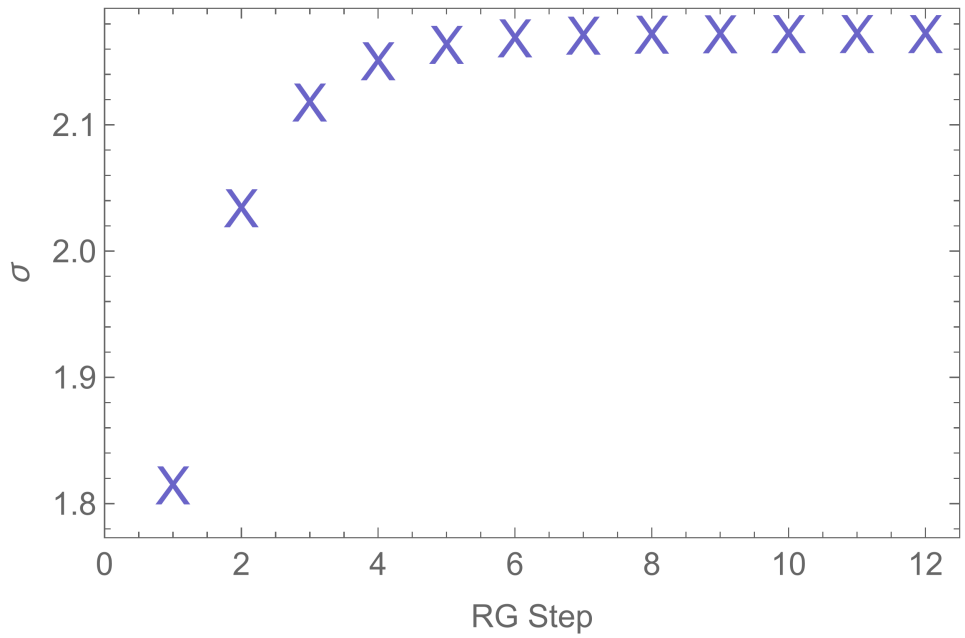

Figure 2.13: Standard deviation of successive $Q(z)$ distributions upon repeated application of the renormalisation transformation. As the distribution approaches the FP distribution, the standard deviation converges to a particular 2.171.

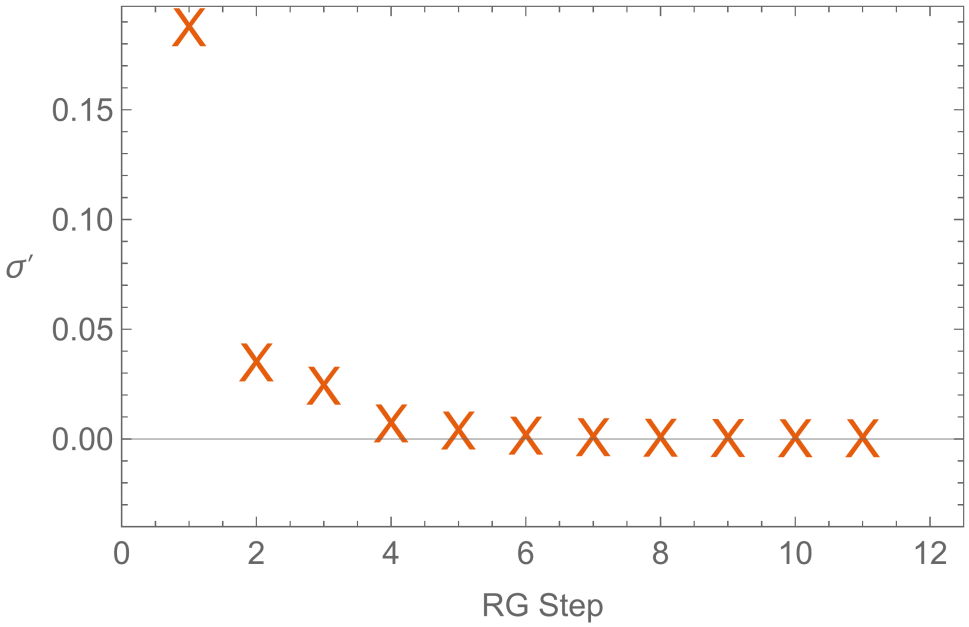

Figure 2.14: The Derivative of the standard deviation of successive $Q(z)$ distributions for increasing renormalisation step. To calculate the values, a pointwise derivative is taken from an interpolation based on splines using the DerivativeFilter Mathematica function. The convergence to 0 as the RG step number increases indicates that the distribution is the FP distribution.

Chapter 3

Improvements on the Real-Space Renormalisation Group Approach

3.1 Improvement on Previous Results

When the critical exponent ν is calculated from the distributions, an essential linear approximation is made between the successive saddle point height distribution maxima and the initial z_0, as was detailed in the previous section. In previous literature, when calculating the critical exponent, the data did not appear to strictly converge to a particular value, instead monotonically decreasing slowly as a function of RG step [75]. Instead, the critical exponent was extracted from the largest RG step at which it was believed the distribution exited the range of validity of the linear approximation. The reason for this was to balance accuracy gains and losses between system size and the linear approximation regime; the critical exponent becomes independent of system size only in the large system limit, while the critical exponent becomes less accurate at large system size as it drifts out of the linear approximation regime. In comparison with previous studies, to allow for more accurate analysis, we use values of z_0 about an order of magnitude smaller than previously used. This results in data which are comparatively more accurate for the same system size. Overall it results in a curve for the critical exponent which converges more uniformly to a particular value. The result of this modification presents a slightly higher value of ν than previously reported with the same method, we find $\nu \approx 2.51$. Furthermore, this value is in greater accordance with more recent numerical calculations using *transfer matrices* [63]. The ν value attained as a function of RG step

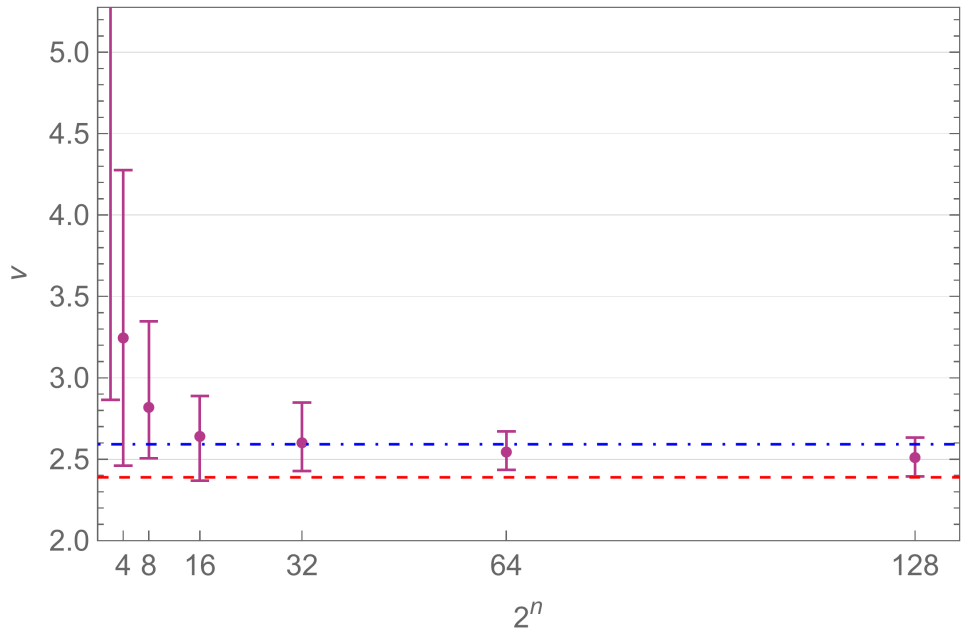

Figure 3.1: A plot of ν as a function of system size, where system size is two to the power of the number of RG steps performed. RG steps one through seven are plotted. Each data point represents three values of z_0 averaged over 10 instances of our method, each instance consisting of 5×10^8 samples. We find a final value of ν to be 2.51 ± 0.11. The dashed red line at 2.39 indicates the result found in [74] and the dashed and dotted blue line at 2.59 indicates the result found in [63].

is displayed in figure 3.1.

3.2 Analytic Formulation in a Single Parameter Basis

While the matrices we have chosen thus far are quite strongly linked to the physical intuition of transmitting and reflecting probability amplitudes, we are not necessarily restricted by constructing a matrix of t or r values. Anything which is in $U(2)$ will produce the same model, albeit in a different basis. To explore this idea in this project we tried using a different basis for the scattering matrices to investigate whether this had any effect on the resultant calculations of the FP distribution or the speed of such calculations. More importantly, we sought to investigate any difference in the critical exponent calculated. Namely, we chose a matrix determined by a single parameter, θ with

$$S = \begin{bmatrix} i\cos\theta & \sin\theta \\ \sin\theta & i\cos\theta \end{bmatrix}.$$

One can easily check such a matrix is unitary. Naturally, we can repeat the same steps as before for this new matrix to find an expression for a renormalised θ. We start with constructing the 10×10 matrix which describes the entire unit cell. Throughout the following derivation, sin and cos will be abbreviated to S and C where an index denotes the saddle point of the scattering parameter, such that e.g. $S_1 = \sin(\theta_1)$. We take this abbreviation to compactly express the matrix describing the RG unit-cell as

$$Ax = b, \tag{3.1}$$

where

$$A = \begin{bmatrix}
1 & 0 & 0 & 0 & 0 & -\mathrm{S}_1 e^{i\phi_{31}} & 0 & 0 & 0 & 0 \\
0 & 1 & 0 & 0 & 0 & -i\mathrm{C}_1 e^{i\phi_{31}} & 0 & 0 & 0 & 0 \\
0 & -i\mathrm{C}_2 e^{i\phi_{12}} & 1 & 0 & 0 & 0 & 0 & -\mathrm{S}_2 e^{i\phi_{42}} & 0 & 0 \\
0 & -\mathrm{S}_2 e^{i\phi_{12}} & 0 & 1 & 0 & 0 & 0 & -\mathrm{S}_2 e^{i\phi_{42}} & 0 & 0 \\
0 & 0 & -\mathrm{S}_3 e^{i\phi_{23}} & 0 & 1 & 0 & 0 & 0 & 0 & -i\mathrm{C}_3 e^{i\phi_{53}} \\
0 & 0 & -i\mathrm{C}_3 e^{i\phi_{23}} & 0 & 0 & 1 & 0 & 0 & 0 & -\mathrm{S}_3 e^{i\phi_{53}} \\
0 & 0 & 0 & 0 & -i\mathrm{C}_4 e^{i\phi_{34}} & 0 & 1 & 0 & 0 & 0 \\
0 & 0 & 0 & 0 & -\mathrm{S}_4 e^{i\phi_{34}} & 0 & 0 & 1 & 0 & 0 \\
-i\mathrm{C}_5 e^{i\phi_{15}} & 0 & 0 & 0 & 0 & 0 & -\mathrm{S}_5 e^{i\phi_{45}} & 0 & 1 & 0 \\
-\mathrm{S}_5 e^{i\phi_{15}} & 0 & 0 & 0 & 0 & 0 & -i\mathrm{C}_5 e^{i\phi_{45}} & 0 & 0 & 1
\end{bmatrix}, \tag{3.2a}$$

$$x = \left[O_1, O_1^*, O_2, O_2^*, O_3, O_3^*, O_4, O_4^*, O_5, O_5^*\right]^T, \tag{3.2b}$$

$$b = \left[i\mathrm{C}_1 I_1, \mathrm{S}_1 I_1, 0, 0, 0, 0, \mathrm{S}_4 I_4^*, i\mathrm{C}_4 I_4^*, 0, 0\right]^T. \tag{3.2c}$$

Identically to the previous section, we invert the matrix and solve for O_5, taking $I_1 = 1$ and $I_4^* = 0$. In the previous section, the derivation for the renormalised coefficients practically stopped here as $t'I' = O'$ so that $O_5 = t'$ and precisely what we measure is our new coefficient. However, this derivation is not satisfactory in the θ basis. In the single parameter basis, we instead find

$$O' = O_5 = i\cos(\theta')I_1 = i\cos(\theta'). \tag{3.3}$$

So to find the renormalised value of θ' we additionally have to take

$$\theta' = \arccos |O_5|. \tag{3.4}$$

Upon doing so we can express the relation between the θ coefficients and the *renormalised θ' coefficient* as

$$\cos\theta' = \left| \frac{\begin{array}{r} -\cos\theta_1 \left(e^{i\Phi_4}\cos\theta_3\cos\theta_4 + i\cos\theta_5\left(e^{i\Phi_3}\sin\theta_2\sin\theta_3\sin\theta_4 - 1\right)\right) \\ - e^{i\Phi_1}\cos\theta_2\cos\theta_3\cos\theta_5 - ie^{i(\Phi_1+\Phi_4)}\cos\theta_4\cos\theta_2 \\ + ie^{i(\Phi_1+\Phi_4-\Phi_2)}\cos\theta_2\cos\theta_4\sin\theta_1\sin\theta_3\sin\theta_5 \end{array}}{\begin{array}{r} e^{i\Phi_4}\cos\theta_3\cos\theta_4\cos\theta_5 + e^{i\Phi_1}\cos\theta_1\cos\theta_2(\cos\theta_3 \\ + ie^{i\Phi_4}\cos\theta_4\cos\theta_5 + i(-1 + e^{i\Phi_3}\sin\theta_2\sin\theta_3\sin\theta_4 \\ + e^{i\Phi_2}\sin\theta_1(\sin\theta_3 - e^{i\Phi_3}\sin\theta_2\sin\theta_4)\sin\theta_5)) \end{array}} \right|. \tag{3.5}$$

3.3 Results upon changing Basis of Scattering Parameters

As was shown in the previous section, by changing the basis of the scattering matrix, we found a much different form for the RG transformation expression for the scattering coefficients. When compared with results from the original basis, no consistent difference was found between the resulting FP distributions. In either basis, the $Q(z)$ distribution has a mean of 0 and converges to a standard deviation of 2.171, see figure 3.2. Furthermore, the time taken to perform a renormalisation step increased upon changing to the single parameter basis. For 100000 samples and 10 RG steps, computing within the t basis took 44.048s while within the θ basis the computation took 44.795s. We conclude that a change of basis does not affect the physics of the CC model transition, and after an analysis of calculation times, we conclude that it does not impact the speed at which one can calculate successive RG transformations.

3.4 Discussion of Results

Our calculated value of ν via the RSRG method is slightly increased compared with previously obtained results on the same model [74]. The likely cause of this disparity lies in the values of z_0 used to calculate the renormalisation flow. As we used a number of configurations two orders of magnitude higher than previous results, this facilitated a more stable analysis at smaller values of z_0 which in turn, more closely conforms to the linear approximation. We have determined that calculating

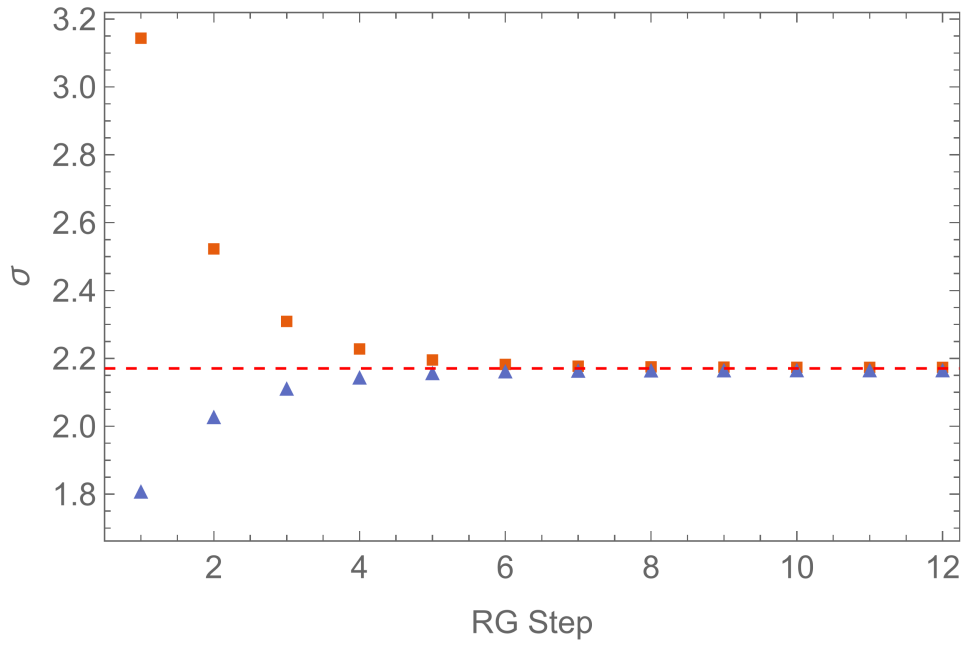

Figure 3.2: The standard deviation of the $Q(z)$ distribution as a function of RG step for both bases considered in the chapter. The orange squares signify the t basis and the blue triangles signify the θ basis. Due to differences in how the distributions are initialised, the standard deviation starts at different values. Upon enough iterations of the renormalisation transformation with a symmetrisation procedure applied to the $Q(z)$ distribution, both distributions converge to the same FP distribution, as is shown by the standard deviations jointly converging to a value of 2.171.

renormalisation transformation using an alternate basis does not have any effect on the resulting FP distribution and a very minimal effect on the computation time.

Chapter 4

Introduction of Geometric Disorder

Following from work detailed in ref. [76], in this section, we wish to structurally implement so-called *geometric disorder* into the model. In this context, geometric disorder takes the form of impurities introduced into the square lattice on which our model resides. In particular, certain saddle points are randomly set to be either fully transmitting or fully reflecting. This particular type of disorder breaks the 2D square lattice symmetry of the system and previously has been associated with a change in critical exponent [76]. It has been previously suggested that the inclusion of *any* geometric disorder changes the universality class of the system. Furthermore, by using the transfer matrix method, the authors of reference [77] found the critical exponent to continuously lower to $\nu \approx 2.3$ when the proportion of disordered nodes reached $\frac{2}{3}$ of the system. Beyond this point, the critical exponent is seen to smoothly increase seemingly without bound. It is then suggested that the new universality class including geometric disorder is that which represents the quantum hall transition more faithfully due to the closer agreement with experiment at the $\frac{2}{3}$ disorder proportion level. What is not yet explained is how the critical exponent smoothly varies from one value to another as this runs in contradiction to the notion of universality classes based on symmetry and topology. This contradiction motivates the following chapter, in which we apply geometric disorder to the RSRG technique to gain further insight into this supposed novel universality class. In particular, we aim to determine whether the continuously changing critical exponent is unique to the implementation via transfer matrix scaling, by attempting to replicate a continuously changing critical exponent via the RSRG method.

4.1 Implementation of Geometric Disorder

In the context of our renormalisation scheme, as before we start with a generated distribution of transmission amplitudes upon which we apply the renormalisation transformation. Upon every transformation with a probability p_c, each saddle point in the RG unit cell has the chance to become entirely transmitting ($t = 1$) or entirely reflecting ($t = 0$). This means with probability $1-2p_c$, the saddle point transmission amplitude will be randomly picked from the previous distribution, as before. It is worth noting that we may also refer to the overall geometric disorder proportion $p = 2p_c$ as p_c relates the probability of a particular node being set to one of $t = 1$ and $t = 0$, not both.

When setting enough t values in the renormalisation transformation to 0, by inspection of equation 2.12 one can see how singularities may often occur. When the $Q(z)$ distribution is viewed after a renormalisation transformation including geometric disorder, discontinuous peaks can be seen far away from the central distribution representing the accumulation of these singularities, see figure 4.1. These peaks theoretically should be at $\pm\infty$ but due to numerical accuracy, when represented in terms of z they appear at around ± 34. When a subsequent renormalisation step is taken including these peaks, the peaks themselves do not change under the renormalisation transformation. As the peaks do not vanish upon successive renormalisation steps, they only increase in size until they overwhelmingly interfere with the determination of the critical FP distribution. Furthermore, a fundamental part of the scaling hypothesis on which the RG method is based supposes scale invariance of the Hamiltonian. The presence of the unphysical peaks breaks the scale invariance as with each renormalisation step, more geometric disorder is effectively added to the system. It is crucial to eliminate the effects of these peaks. To ensure this, we remove these discontinuous spikes by modifying the bounds imposed when calculating the distribution of z values. This results in geometric disorder being distributed evenly across all length scales, as required. Quantitatively, we set the bounds of z values between -25 and $+25$. In terms of t the bounds equate to 1.39×10^{-11} and $1 - 1.39 \times 10^{-11}$, which justifies our use for such bounds, as they represent a truly minuscule proportion of the overall data while still effectively blocking out the unphysical peaks.

With these modifications in place, we find the FP distribution as before. The consecutive application of the renormalisation transformation and a symmetrisation procedure between steps indeed results in an FP distribution when varying the value of p. This is shown by the converging of mean-square deviation between successive

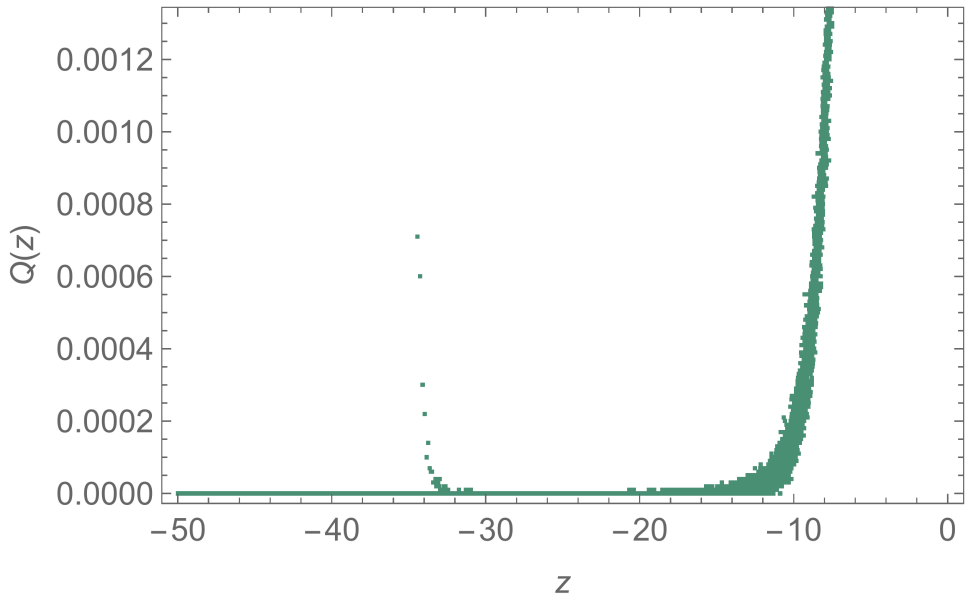

Figure 4.1: The $Q(z)$ distribution between $-50 \leq z \leq 0$ after a renormalisation transformation incorporating geometric disorder has been applied. A discontinuous spike in the distribution is seen at roughly $z = -34$. When we set the z cutoff such that $|z| \leq 25$, we stop the discontinuous spikes from influencing further distributions, while still including the part of the distribution which corresponds to the Chalker-Coddington model.

distributions. The introduction of geometric disorder has no effect on the mean value of z at the critical fixed point, as the conducting limit is at $z = 0$. The introduction of geometric disorder notably increases the number of steps required to converge upon an FP distribution. This is shown in figure 4.2 with Δ plotted against iteration number for varying values of $p_c = \frac{1}{2}p$. Additionally, the shape of the FP distribution changes depending on p_c, as shown by the change in standard deviation converged upon for different p_c values in figure 4.3. For larger proportions of geometric disorder, we note a consistent increase in the standard deviation of the FP distribution.

Once the FP distribution is found, we use our previously deployed method to estimate the value of the critical exponent. After shifting the FP distribution of saddle point heights by a value z_0 we iterate the RG transformation upon the resulting distribution and use the maxima to calculate the critical exponent via equation (2.21).

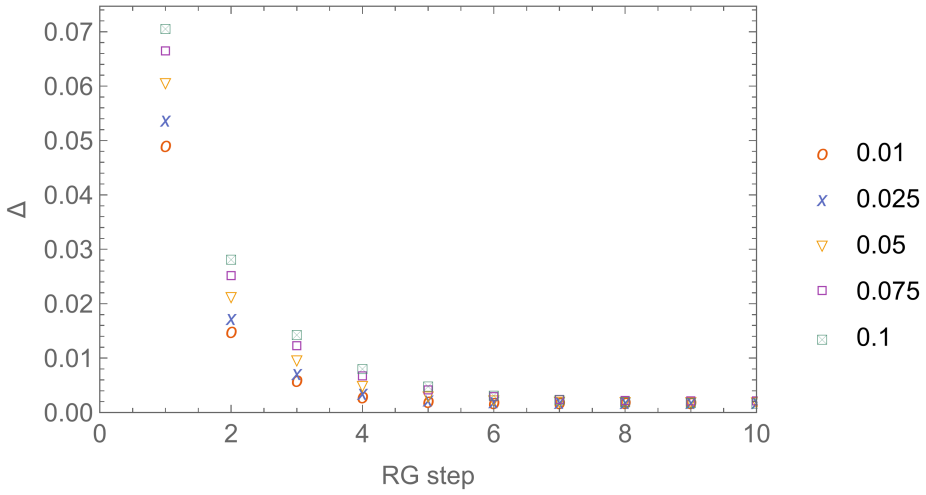

Figure 4.2: A Comparison of Δ (see figure 2.12) values as the number of RG steps increases, plotted for multiple values of p_c as indicated in the legend. For all values of geometric disorder, the $Q(z)$ distribution converges. As the proportion of geometric disorder is increased, more renormalisation steps are required for the distribution to converge.

4.2 Transformation between presented Results and Current Literature

When comparing our results with the available literature, there exists a disparity in not only the form of the resulting curve but additionally the range of values we obtain. However, as of yet, we have not factored in the simplified geometry of the RG unit cell. Within the unit cell, there are four nodes which are essentially 'skipped over' to maintain self-consistency upon the renormalisation transformation. Our depiction of the unit cell does not wholly represent a square 2D lattice. Our interpretation of this is that the unit cell already exhibits geometric disorder with a proportion of $\frac{4}{9}$ as effectively, four of what would be nine nodes comprising a square unit cell are instead set to either $t = 0$ or $t = 1$. The takeaway is that when we present our results for '$p_c = 0$' geometric disorder, in reality, these data represent a $p_c = \frac{2}{9}$ proportion of geometric disorder. Thus all data of our must be translated along the p_c axis by $\frac{2}{9}$. To maintain a consistent and physical upper bound, we now have to apply a scaling factor to ensure that the purely disordered limit coincides with that of other literature. This must be $\frac{5}{18}$ such that $p' \in [\frac{2}{9}, \frac{1}{2}]$. We then find that the transformation which satisfies these conditions takes the form

$$p' = \frac{5}{18}p + \frac{2}{9}, \tag{4.1}$$

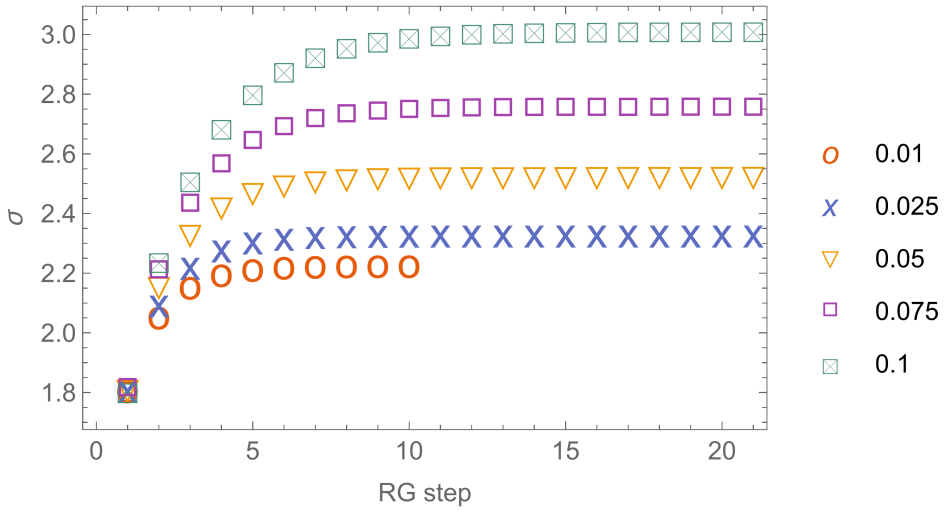

Figure 4.3: A Comparison of σ (see figure 2.13) values as the number of RG steps increases, plotted for multiple values of p_c as indicated in the legend. Increasing the value of p_c appears to increase the value of σ in the corresponding FP distribution.

where p' is the geometric disorder site probability scaled for easy comparison with reference [77] and p is the overall proportion of geometric disorder we implement. Once data have been mapped onto this parameter, we find that our value of ν at $p = 0$ maps very close to the value of ν found at $p_c = \frac{2}{9}$ in external literature. This gives credence to our determination of the critical exponent at '0' disorder, and our transformation between the two schemes. Our results with a comparison to the data found in reference [77] are shown in figure 4.4.

4.3 Alternate Approach accounting for Non-Uniform Significance of Nodes within the Unit Cell

Due to the stark incompatibility between what was previously found and what was found using the RSRG technique, we further wish to determine whether alternate applications of geometric disorder produce differing results. Within the RG unit cell, a significant determiner of the overall flow within the cell is the central node. When the central node is randomly assigned to $t = 0$ or $t = 1$, it has a much more severe effect than surrounding nodes on the renormalised parameters. We thus decided to exclude the central node from the possibility of being affected by geometric disorder. With this modification, we followed the steps as described before identically. This

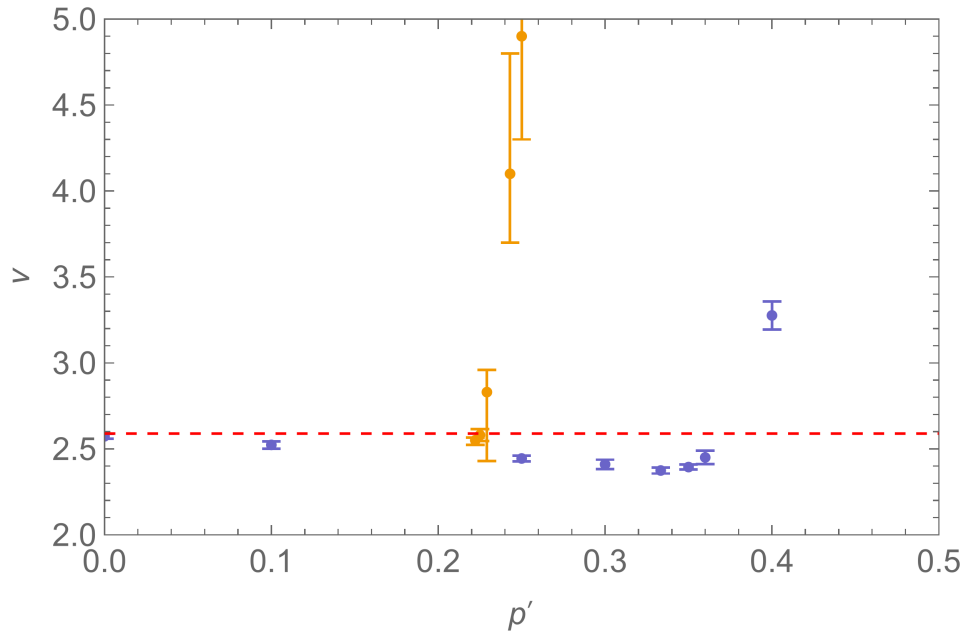

Figure 4.4: As a function of geometric disorder p', our results for ν displayed in orange, are compared with the data in [77], in blue. The red dashed line at 2.59 represents the value of ν found in [63], included as a visual guide.

modification also requires a slightly different parameter transformation as now

$$p' = \frac{2}{9} + p\frac{2}{9}. \tag{4.2}$$

When transformed, the modification resulted in an even steeper curve for ν than previously, as shown in figure 4.6, only suggesting that such a modification brings us further away from the phenomena as described in reference [76]. Our numerical results for ν both with and without this modification are displayed in table 4.1.

4.4 Continuously changing Critical Exponent

One question not addressed throughout this work is why, when geometric disorder is added to the model, the critical exponent changes continuously as a function of disorder proportion. This seems to inherently contradict the idea of universality and thus in this section, we present a couple of possible explanations as to why a continuous line of critical exponents may be found.

Primarily, as briefly mentioned before, by using a conformal field theoretic approach, Zirnbauer in reference [64] argues that the relevant observables have only marginal perturbative corrections. In principle, this implies that for the conformal field the-

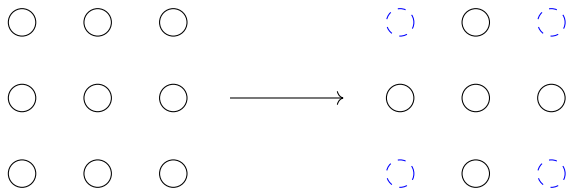

Figure 4.5: A comparison showing where we have 'skipped over' nodes in the formation of the RG unit cell, as depicted in figure 2.4. The left indicates a section of the infinite 2D lattice, whereas the right shows our representation to be used as an RG unit cell. Moving from the left to the right, four nodes are not included, which motivates the transformation represented by equation (4.1).

Without Modification				With Modification			
p	p_c	p'	ν	p	p_c	p'	ν
0	0	0.222	$2.51^{+0.11}_{-0.11}$	0	0	0.222	$2.51^{+0.11}_{-0.11}$
0.02	0.01	0.225	$2.57^{+0.05}_{-0.018}$	0.2	0.1	0.244	$4.2^{+0.4}_{-0.4}$
0.05	0.025	0.229	$2.83^{+0.13}_{-0.4}$	0.4	0.2	0.267	$11.9^{+1.2}_{-1.4}$
0.15	0.075	0.243	$4.1^{+0.7}_{-0.4}$	0.6	0.3	0.289	25^{+11}_{-9}
0.2	0.1	0.25	$4.9^{+0.6}_{-0.6}$				

Table 4.1: Table of values attained for the critical exponent ν when introducing geometric disorder at varying proportion levels p.

oretic model of the quantum Hall transition, the critical exponent governing the localisation length is not well defined. A further implication of this is a continuous line of critical exponents forming [78–81]. We suggest that the geometric disorder may manifest this behaviour.

Alternatively, another scenario resulting in non-universal continuous exponents arises when two models with distinct scaling behaviour are mixed [82]. This phenomenon has been found in multiple percolation models [83, 84], which could provide insight into the Chalker-Coddington quantum percolation model. Indeed when we add geometric disorder we are changing from a quantum percolation model to a classical percolation model. The classical extreme of the model has previously received study [85], although we have not found a satisfactory marriage between the results of the classical model and our results found here.

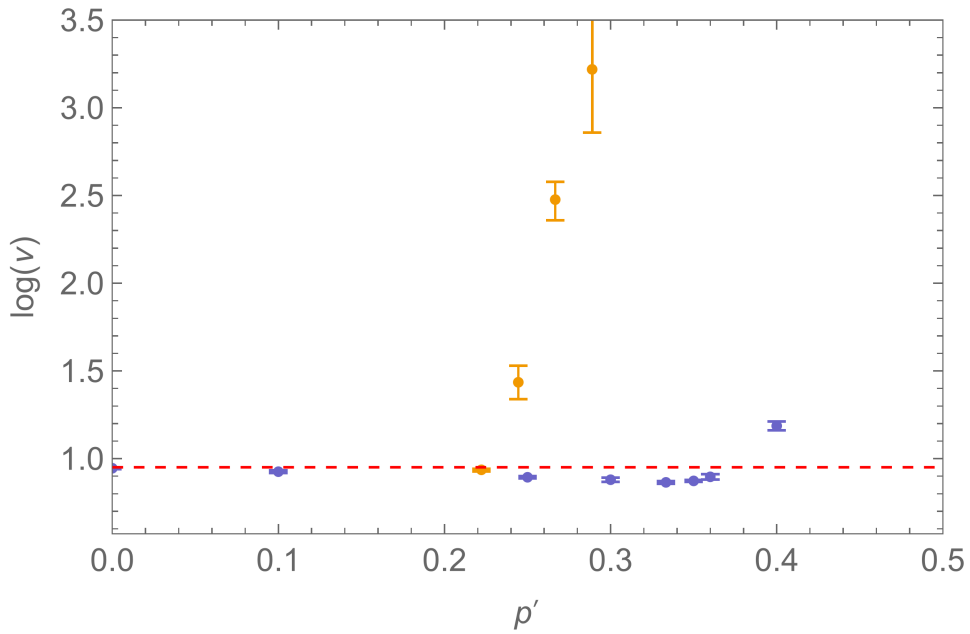

Figure 4.6: As a function of geometric disorder p' in our alternate geometric disorder implementation, values for ν are displayed on a logarithmic scale. The values calculated in this thesis are in orange, compared with the data from [77], in blue. The red dashed line at $\ln(2.59) = 0.952$ represents the value of ν found in [63], included as a visual guide.

Chapter 5

Application to Time-Reversal Invariant Topological Insulators

To make a model for a TRI topological insulator, we can simply extend the Chalker-Coddington model. By introducing a time-reversed pathway between each node, we form the pathways for the Kramer's pair traversing the network. From our previous discussion on time-reversal invariance, the existence of Kramer's pairs is sufficient to describe the TRI system. In this section we will denote the two species of electron as electrons with opposite spin, that is $\uparrow$ and $\downarrow$. Instead of two input edges and two output edges, there are four, as shown in figure 5.1. When an electron passes into the node, there are now three different outcomes. The electron can reflect or transmit through the saddle point as previously seen, or it can additionally flip its spin and travel directly through the node. These scenarios with their respective probability amplitudes are displayed in figure 5.2

5.1 Scattering Matrix Representation

Due to the additional connecting edges to and from each node, the scattering matrix S also will take on a new form, consisting of 4×4 entries instead of 2×2. Our new scattering matrix will additionally have to preserve time-reversal invariance, as well as meet the unitarity conditions previously described. Under these conditions alone, we would describe nothing more than two Chalker-Coddington models stacked on top of one another, hence the introduction of a *spin mixing term* within the scattering matrix. This allows for the wavefunctions to alter the dynamics of their

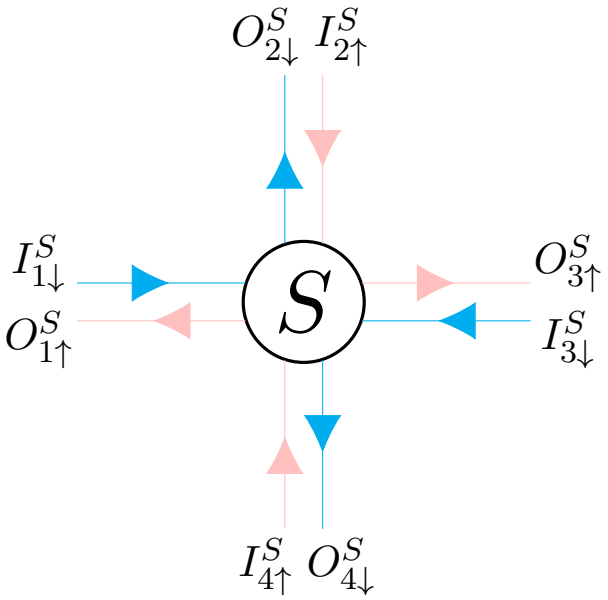

Figure 5.1: A TRI saddle point represented by the node S. Each edge surrounding the node represents an equipotential with blue edges indicating spin-down equipotentials while pink edges indicate spin-up equipotentials. Each edge is indexed by the name of the saddle point (upper index), the orientation of the edge in relation to the saddle point and the spin species of the electrons travelling through (lower indices). Each side of the node has both incoming and outgoing edges.

time-reversed partners. The resulting matrix takes the form

$$S = \begin{bmatrix} 0 & i\cos(\phi)\cos(\theta) & \cos(\phi)\sin(\theta) & \sin(\theta) \\ i\cos(\phi)\cos(\theta) & 0 & -\sin(\phi) & \cos(\phi)\sin(\theta) \\ \cos(\phi)\sin(\theta) & \sin(\phi) & 0 & i\cos(\phi)\cos(\theta) \\ -\sin(\phi) & \cos(\phi)\sin(\theta) & i\cos(\phi)\cos(\theta) & 0 \end{bmatrix}, \tag{5.1}$$

where θ is the regular scattering parameter and ϕ is our introduced spin mixing angle. With reference to figure 5.1, with this scattering matrix, the input and

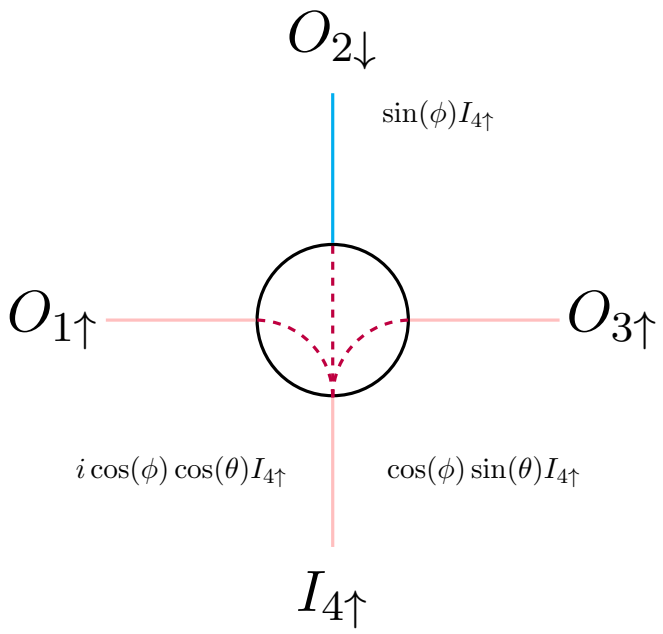

Figure 5.2: A simplified TRI scattering node showing one incoming edge south of the node and the three outgoing edges to which amplitude could transfer. The edges are labelled as in figure 5.1 with the corresponding probability amplitudes of that particular traversal in terms of the spin mixing angle ϕ and the scattering angle θ.

output edges are related by

$$\begin{bmatrix} 0 & i\cos(\phi)\cos(\theta) & \cos(\phi)\sin(\theta) & \sin(\theta) \\ i\cos(\phi)\cos(\theta) & 0 & -\sin(\phi) & \cos(\phi)\sin(\theta) \\ \cos(\phi)\sin(\theta) & \sin(\phi) & 0 & i\cos(\phi)\cos(\theta) \\ -\sin(\phi) & \cos(\phi)\sin(\theta) & i\cos(\phi)\cos(\theta) & 0 \end{bmatrix} \begin{bmatrix} I_{1\downarrow} \\ I_{4\uparrow} \\ I_{2\uparrow} \\ I_{3\downarrow} \end{bmatrix} = \begin{bmatrix} O_{1\uparrow} \\ O_{4\downarrow} \\ O_{2\downarrow} \\ O_{3\uparrow} \end{bmatrix}. \tag{5.2}$$

5.2 Application of the Real-Space Renormalisation Group

As was demonstrated in the regular Chalker-Coddington scenario in section 2.2, we will attempt an RSRG approach to extract the critical exponent of the localisation length. We start by constructing our unit cell as before, but with our newly defined TRI nodes. The result of this is depicted in figure 5.3. It is important to note that because of time-reversal symmetry, the phase accumulated across any link will be

equal to the negative of the phase accumulated across the time-reversed link. We then proceed to build up a system of equations relating the inputs and outputs of each cell to one another. Because of the time-reversal invariance, we have removed the potential for different centre orientations and thus can be oriented in any way to carry out the calculations. The system of equations can be expressed as a matrix equation to solve, as demonstrated in section 2.2. Unfortunately, the resulting 20×20 matrix is simply too big to display on one page, so it is instead described in block form in section A. Similarly, the analytic solution to the matrix equation is too large to fit within this thesis, thus the formula for the exact renormalisation transformation will also be omitted. In reference to the analytic solution, within Mathematica, after multiple uses of the Simplify function at different depth levels using the ParallelMap function, the smallest form for the renormalisation transformation formula contained 129271 indivisible subexpressions, calculated with the LeafCount function also within Mathematica. In lieu of a direct expression, we will denote the transformation $F(\theta^I, \theta^{II}, \theta^{III}, \theta^{IV}, \theta^V, \{\gamma\})$ where $\{\gamma\}$ represents the set of random phases between links. Instead of using the analytical expression to calculate renormalisation steps, we can apply a straightforward approach by randomising the free parameters within the 20×20 matrix and then inverting this matrix numerically before reading off the desired output measurements. calculating the renormalisation transformation via inverting the matrix proved much faster than via the analytical transformation. Doing so was still slower than previous, more simple models and thus in this section, the data are calculated with 10^7 samples.

Before performing novel calculations with the inverted matrix, to check we have found the correct transformation we can simplify the final renormalisation equation back to the original model and compare it against what was originally found. We can set all spin mixing angles to $\phi = 0$ and additionally set only one electron species to be flowing through the system. We find the resulting equation to be of a much simpler form than when calculated in full generality and so can be used freely to compare to previously derived transformations. We compare the values of the renormalisation transformations for the original and TRI model by setting all renormalised parameters $\{\theta^I, \ldots, \theta^V\}$ equal to one another and sweeping through the domain $0 \leq \theta < \pi$, the results in figure 5.4, showing the exact match between the two.

5.3 Corrections to the Renormalisation Transformation due to Reversed Propagation

What our defined function represents within the unit cell depends on certain initial conditions and external parameters. In the original Chalker-Coddington case, we initialise with one input $I = 1, I^* = 0$ and collect data from one of the outputs. Due to the simplicity of the network model, the renormalised parameter t can be found immediately as $O = t'I = t'$. When re-parameterising in terms of θ we had to account for the trigonometric term in this equation and take the inverse cos to retrieve the renormalised $\theta' = \arccos O'$. In the present case if we measure an output $O_{4\uparrow}$, in terms of the larger unit cell,

$$|O_{4\uparrow}| = |\cos(\phi)\sin(\theta')I_{3\uparrow} + \sin(\phi)I_{2\downarrow} + i\cos(\phi)\cos(\theta')I_{1\uparrow}|. \tag{5.3}$$

To access the renormalised parameter we need to take a few steps. The first is setting the correct inputs and taking values from the correct outputs. Here we set $I_{3\uparrow} \to 1$ and take values from $|O_{r\uparrow}|$. From the above equation, one may assume that we can simplify and find that

$$\theta' = \frac{\arcsin(|O_{4\uparrow}|)}{\cos(\phi)}, \tag{5.4}$$

where ϕ is what we have previously globally set it to. This is unfortunately an incomplete derivation and results in a distribution of θ values which is not normalisable. The error is due to a slight inconsistency when transforming from the individual cell to the larger unit cell. In the original node as emphasised before (see figure 5.2, every input has 3 possible directions to exit away from. In other words, the input cannot leave through the same direction it came. This is not true for the larger unit cell. An incoming electron could enter through the $\downarrow$ spin channel, propagate through the unit cell, switch to the $\uparrow$ spin channel and subsequently leave through the same node it entered the system from. Simply stated, unitarity for the entire unit cell only holds if we take into account the amplitude lost due to this effect. Put more concretely, for a single node

$$\sqrt{|O_{1\uparrow}|^2 + |O_{3\uparrow}|^2 + |O_{2\downarrow}|^2} = \sqrt{|I_{4\uparrow}|^2}, \tag{5.5}$$

however for the unit cell,

$$\sqrt{|O_{1\uparrow}|^2 + |O_{3\uparrow}|^2 + |O_{2\downarrow}|^2 + |O_{4\downarrow}|^2} = \sqrt{|I_{4\uparrow}|^2}. \tag{5.6}$$

This additional factor is not accounted for in the general matrix describing the saddle points. To account for the additional factor, one solution that provides suitable results is absorbing it into the $|O_{2\downarrow}|$ term. When a renormalisation transformation is computed for a particular spin mixing angle ϕ, the effect of the amplitude loss can be thought of as an 'effective' change to ϕ, i.e. if some of the amplitude is lost, this is equivalent to more electrons switching spins and exiting via the opposite spin channel. Considering we set $I_{r\uparrow} \to 1$, we can determine the effective ϕ, denoted ϕ_c, by calculating $|O_{2\downarrow}|$ as for the single node,

$$|O_{2\downarrow}| = |\sin(\phi_c) I_{4_\uparrow}| = |\sin(\phi_c))|. \tag{5.7}$$

Once we have calculated ϕ_c for the unit cell, we can subsequently calculate a renormalised θ' via

$$F(\theta^I, \theta^{II}, \theta^{III}, \theta^{IV}, \theta^V, \{\gamma\}) = \theta' = \arcsin \frac{|O_{4\uparrow}|}{\cos(\phi_c)} = \arcsin \frac{|O_{4\uparrow}|}{\sqrt{1 - |O_{2\downarrow}|^2}}. \tag{5.8}$$

We have thus defined the renormalisation transformation from which we can calculate RG steps. We show a familiar form of t distribution in figure 5.5 and we show how the distribution of θ changes after multiple applications of the transformation in figure 5.6.

5.4 Discussion

While we have not found an FP distribution from our renormalisation transformation, we have found that the successive distributions indeed change with varying the spin mixing parameter ϕ. As we have successfully found a renormalisation transformation for the TRI model, we believe that an FP distribution can also be found. Once this is achieved, calculating the critical exponent ν will be a matter of routine as set out in section 2.2.3. There exists extensive literature regarding the quantum spin-Hall effect, including calculations of ν from which a comparison can be made to examine the validity of any future results [86, 87].

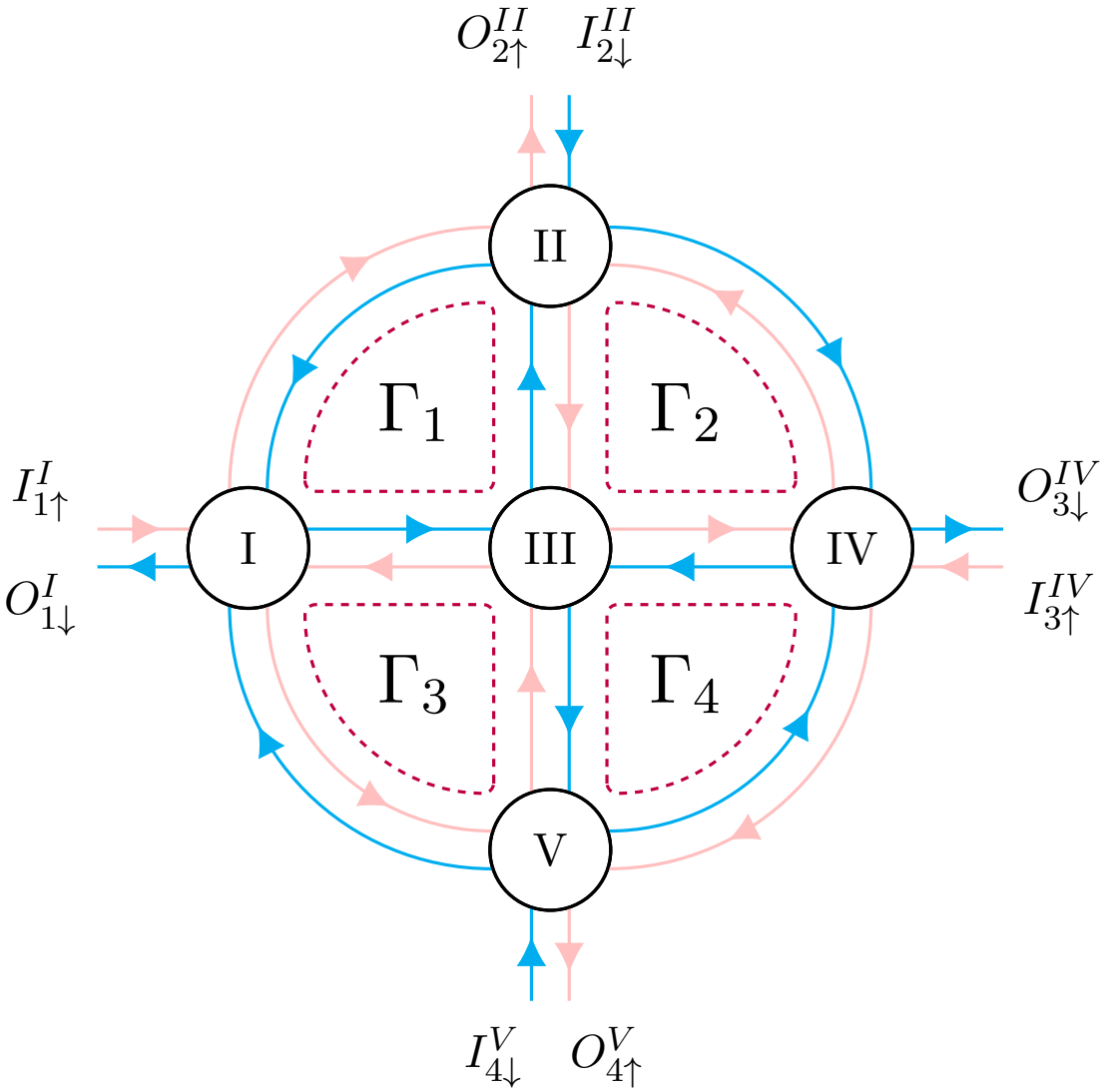

Figure 5.3: The modified RSRG unit cell (see figure 2.4) to satisfy time-reversal invariance. The unit cell consists of the same form, however, each node is instead a TRI node. Edges are notated in agreement with figure 5.1, where the upper index is the Roman numeral of the node that the edge belongs to. Accrued phases along loops of the unit cell are denoted with Γ.

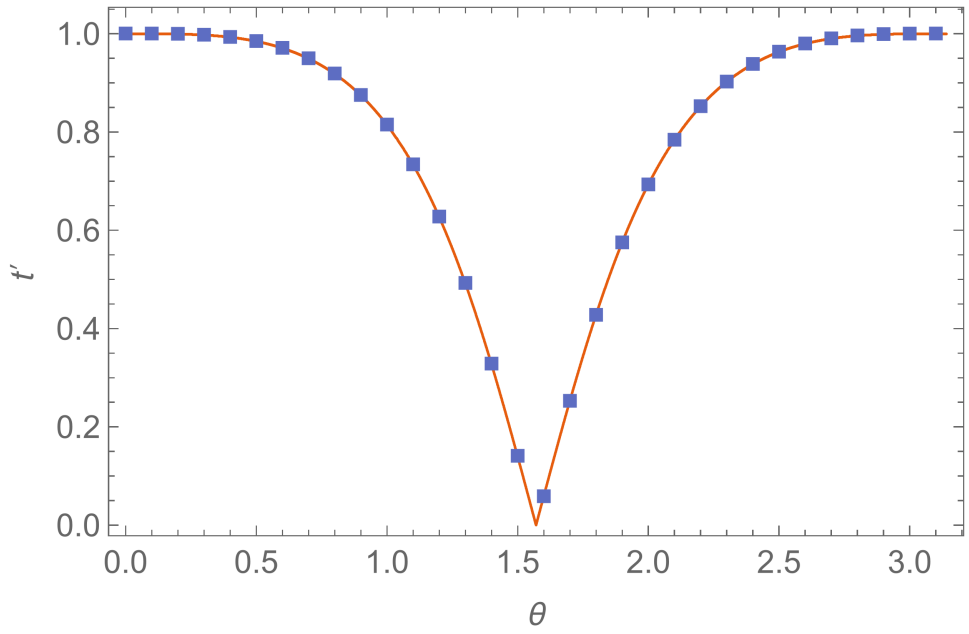

Figure 5.4: In orange, the graph of $F(\theta)$ in terms of t assuming that $\phi = 0$ and all scattering angles θ are equivalent. In blue, the corresponding data for the transformation defined by equation (3.5). Plot points are omitted from the latter for visual clarity.

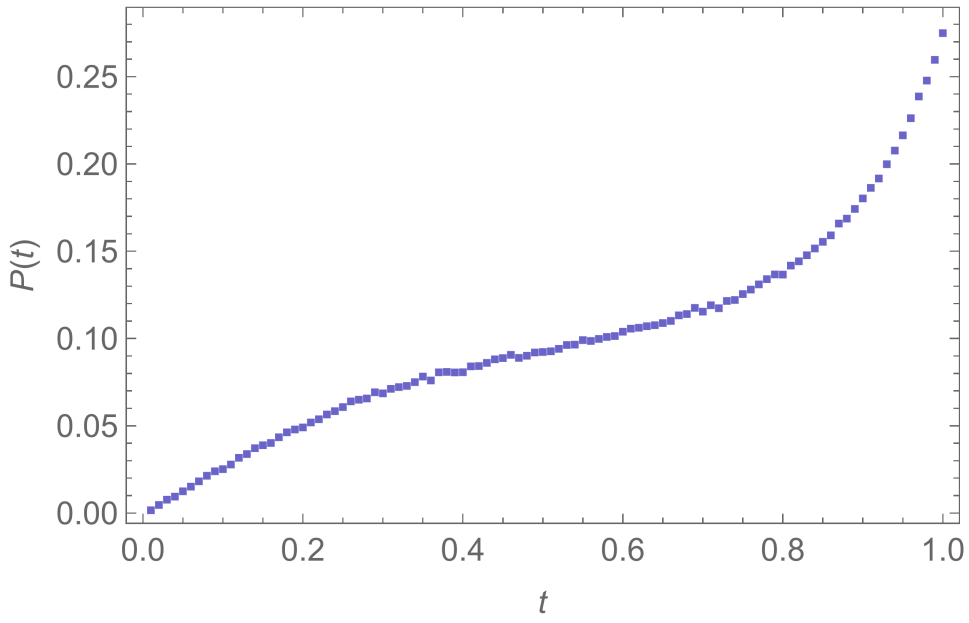

Figure 5.5: The $P(t) = P(\cos[\theta])$ distribution calculated from the approach detailed in this chapter. The distribution takes a similar form to figure 2.6.

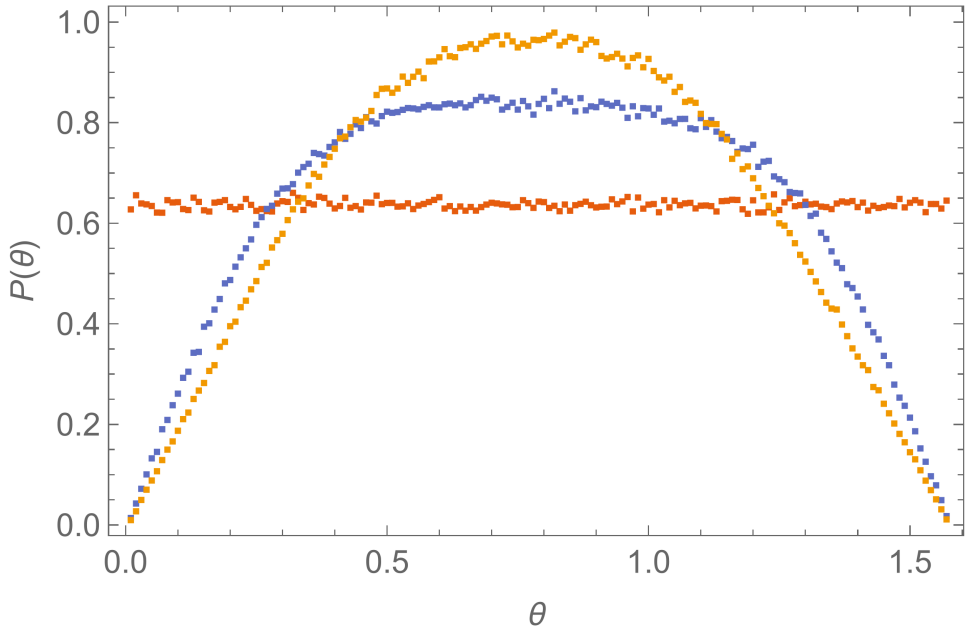

Figure 5.6: The $P(\theta)$ distribution upon the first two applications of the TRI renormalisation transformation. The initial distribution(red) is uniform in θ and the two consecutive renormalisation steps(blue and orange, respectively) form a distribution centred on $\frac{\pi}{2}$ and decreasing full width at half maximum.

Chapter 6

Conclusion

6.1 Summary of Work

Our work provides a background of the quantum Hall effect, with a small detour into the topological aspects. In particular, we form the link between a topological invariant based on the band structure and the transverse conductance in the quantum Hall effect. We present the topological similarities between the quantum Hall and quantum spin-Hall effect from the perspective of topological invariants. We cover the broad motivation behind the RG and why it becomes useful for the determination of critical properties. We explain the particular method used throughout this thesis, the RSRG and its application to the Chalker-Coddington model. Due to an increased number of samples used throughout our calculations, we were able to calculate the RG flow for smaller z_0 values. In turn, our results adhere closer to the linear scaling supposed by the method. We find that in doing so, an elevated estimate for the critical exponent $\nu \approx 2.51$ is numerically determined, which is closer to other numerically determined values of around $\nu = 2.59$. The RSRG method was modified such that scattering matrices were formed in a different basis, involving trigonometric terms. Comparisons between the results from both bases indicate a minimal impact from changing the basis. Additionally, we found that between both bases, the difference between computing time for a renormalisation step was negligible. The RSRG method is extended to include so called geometric disorder, proposed by Gruzberg et al [76], where lattice impurities are manifest across the system. We find that a straightforward adaptation of the RSRG technique including geometric disorder leads to the formation of discontinuous peaks in the $Q(z)$ distribution. The presence of the peaks within the distribution represents singularities occurring in the renormalisation transformation. We note that these peaks in

the distribution increase in size under each renormalisation transformation, signifying a break in scale invariance and leading to a trivial distribution upon sufficient renormalisation steps. To circumvent this issue, we manually restrict the range of z values. With our implementation of geometric disorder, we successfully find FP distributions. Furthermore, we find that increasing the proportion of geometric disorder within the system is linked to an increase in the standard deviation of the FP $Q(z)$ distribution. From the FP distributions, we utilise two implementations of geometric disorder, both of which find a continuously changing critical exponent, in agreement with reference [77]. Despite this, the precise values of ν found are shown to differ strongly between our work and that in reference [77]. We suggest possibilities behind the manifestation of a continuously changing critical exponent. Namely, we suggest that by including geometric disorder, the model becomes a mix between two separate percolation models with different critical properties, causing the blended model to shift between either two. We then extend the RSRG method to a time-reversal invariant Chalker-Coddington model. We find that compared with previous variations of the RSRG, an additional correction is needed to derive the renormalisation transformation. Once the correction is factored in, we successfully find the real-space renormalisation transformation for the time-reversal invariant Chalker-Coddington model.

6.2 Further Work

As all work in this thesis was completed within Mathematica, our work could be extended by using a language such as C++ or Fortran, in which more optimised code could be made and used to increase the precision of all results. The precise nature of the continuous line of critical exponents seen in the geometrically disordered Chalker-Coddington model deserves more attention and analysis of the mechanisms supporting the breakdown of universality. While we have presented potential explanations, none are clearly and exclusively linked to this particular scenario and thus additional work is required. Furthermore, a stronger analysis of the precise effect that different implementations of geometric disorder have is required to gain a greater understanding of the effects of geometric disorder. Due to the time restriction placed upon this work, sufficient analysis of the TRI CC model was not carried out, although with the formulation of the correct RG transformation, this provides a direct line of work as a continuation of this thesis. This work also opens up the avenue of further extension to alternate symmetry classes for the RSRG technique, although no other such classes have been explored throughout this thesis. A poten-

tial extension of our work was identified in a 3D variant of the Chalker-Coddington model shown to exhibit a strong topological insulator phase [88]. Currently, the formulation of the RSRG method in this context remains challenging. The renormalisation transformation requires the existence of a unit cell which can 'tile' to build up the overall system, whilst being self-similar. The extended 3D model does not consist of uniform nodes to tile with and thus we are currently working on alternative implementations which satisfy all imposed restrictions on the unit cell.

Appendix A

Matrix representing the Time-Reversal Invariant Chalker-Coddington Real Space Renormalisation Group Unit Cell

In section 5, we considered the TRI Chalker-Coddington model and omitted the matrix representing the RG unit cell due to space restrictions. Here we describe the matrix in its entirety. With ψ_q representing the spin mixing angle for node number q, θ_q representing the scattering angle for node number q and ϕ_{rs} representing the phase accrued between node r and s, the matrix representing the time-reversal invariant Chalker-Coddington real space renormalisation group unit cell can be expressed in block form

$$X = \begin{bmatrix} \mathbf{A} & \mathbf{B} \\ \mathbf{C} & \mathbf{D} \end{bmatrix}. \tag{A.1}$$

In the following, $\cos(Z)$ and $\sin(Z)$ are abbreviated to C_Z and S_Z, respectively. With this in mind, we find

$$\mathbf{A} =$$

$$\begin{bmatrix}
1 & 0 & 0 & 0 & 0 & 0 & 0 & 0 & -C_{\psi_1} S_{\theta_1} e^{-i\phi_{13}} & 0 \\
0 & 1 & 0 & 0 & 0 & -iC_{\psi_1} C_{\theta_1} e^{i\phi_{21}} & 0 & 0 & S_{\psi_1} e^{-i\phi_{13}} & 0 \\
0 & 0 & 1 & 0 & 0 & -C_{\psi_1} S_{\theta_1} e^{i\phi_{21}} & 0 & 0 & 0 & 0 \\
0 & 0 & 0 & 1 & 0 & S_{\psi_1} e^{i\phi_{21}} & 0 & 0 & -iC_{\psi_1} C_{\theta_1} e^{-i\phi_{13}} & 0 \\
-iC_{\psi_2} C_{\theta_2} e^{-i\phi_{21}} & 0 & 0 & 0 & 1 & 0 & 0 & 0 & 0 & 0 \\
0 & 0 & 0 & 0 & 0 & 1 & 0 & 0 & 0 & 0 \\
-S_{\psi_2} e^{-i\phi_{21}} & 0 & 0 & 0 & 0 & 0 & 1 & 0 & 0 & 0 \\
-C_{\psi_2} S_{\theta_2} e^{-i\phi_{21}} & 0 & 0 & 0 & 0 & 0 & 0 & 1 & 0 & 0 \\
0 & 0 & 0 & 0 & 0 & 0 & 0 & -C_{\psi_3} S_{\theta_3} e^{-i\phi_{32}} & 1 & 0 \\
0 & 0 & -iC_{\psi_3} C_{\theta_3} e^{i\phi_{13}} & 0 & 0 & 0 & 0 & S_{\psi_3} e^{-i\phi_{32}} & 0 & 1
\end{bmatrix} \tag{A.2}$$

$$\mathbf{B} =$$

$$\begin{bmatrix}
0 & 0 & 0 & 0 & 0 & 0 & -S_{\psi_1} e^{i\phi_{51}} & 0 & 0 \\
0 & 0 & 0 & 0 & 0 & 0 & -C_{\psi_1} S_{\theta_1} e^{i\phi_{51}} & 0 & 0 \\
0 & 0 & 0 & 0 & 0 & 0 & -iC_{\psi_1} C_{\theta_1} e^{i\phi_{51}} & 0 & 0 \\
0 & 0 & 0 & 0 & 0 & 0 & 0 & 0 & 0 \\
-S_{\psi_2} e^{i\phi_{32}} & 0 & -C_{\psi_2} S_{\theta_2} e^{-i\phi_{24}} & 0 & 0 & 0 & 0 & 0 & 0 \\
-C_{\psi_2} S_{\theta_2} e^{i\phi_{32}} & 0 & S_{\psi_2} e^{-i\phi_{24}} & 0 & 0 & 0 & 0 & 0 & 0 \\
-iC_{\psi_2} C_{\theta_2} e^{i\phi_{32}} & 0 & 0 & 0 & 0 & 0 & 0 & 0 & 0 \\
0 & 0 & -iC_{\psi_2} C_{\theta_2} e^{-i\phi_{24}} & 0 & 0 & 0 & 0 & 0 & 0 \\
0 & 0 & 0 & -S_{\psi_3} e^{i\phi_{43}} & 0 & -iC_{\psi_3} C_{\theta_3} e^{-i\phi_{35}} & 0 & 0 & 0 \\
0 & 0 & 0 & -C_{\psi_3} S_{\theta_3} e^{i\phi_{43}} & 0 & 0 & 0 & 0 & 0
\end{bmatrix} \tag{A.3}$$

$$\mathbf{C} =$$

$$\begin{bmatrix}
0\,0 & -C_{\psi_3}S_{\theta_3}e^{i\phi_{13}} & 0 & 0\,0 & 0 & 0 & 0 & 0 \\
0\,0 & S_{\psi_3}e^{i\phi_{13}} & 0 & 0\,0 & 0 & -iC_{\psi_3}C_{\theta_3}e^{-i\phi_{32}} & 0 & 0 \\
0\,0 & 0 & 0 & 0\,0 & 0 & 0 & 0 & 0 \\
0\,0 & 0 & 0 & 0\,0 & -iC_{\psi_4}C_{\theta_4}e^{i\phi_{24}} & 0 & 0 & 0 \\
0\,0 & 0 & 0 & 0\,0 & -C_{\psi_4}S_{\theta_4}e^{i\phi_{24}} & 0 & 0 & 0 \\
0\,0 & 0 & 0 & 0\,0 & S_{\psi_4}e^{i\phi_{24}} & 0 & 0 & 0 \\
0\,0 & 0 & -iC_{\psi_5}C_{\theta_5}e^{-i\phi_{51}} & 0\,0 & 0 & 0 & 0 & 0 \\
0\,0 & 0 & 0 & 0\,0 & 0 & 0 & 0 & -iC_{\psi_5}C_{\theta_5}e^{i\phi_{35}} \\
0\,0 & 0 & -S_{\psi_5}e^{-i\phi_{51}} & 0\,0 & 0 & 0 & 0 & -C_{\psi_5}S_{\theta_5}e^{i\phi_{35}} \\
0\,0 & 0 & -C_{\psi_5}S_{\theta_5}e^{-i\phi_{51}} & 0\,0 & 0 & 0 & 0 & S_{\psi_5}e^{i\phi_{35}}
\end{bmatrix} \tag{A.4}$$

$$\mathbf{D} =$$

$$\begin{bmatrix}
1 & 0 & 0 & -iC_{\psi_3}C_{\theta_3}e^{i\phi_{43}} & 0 & 0 & -S_{\psi_3}e^{-i\phi_{35}} & 0 & 0 & 0 \\
0 & 1 & 0 & 0 & 0 & 0 & -C_{\psi_3}S_{\theta_3}e^{-i\phi_{35}} & 0 & 0 & 0 \\
0 & -iC_{\psi_4}C_{\theta_4}e^{-i\phi_{43}} & 1 & 0 & 0 & 0 & 0 & 0 & -S_{\psi_4}e^{i\phi_{54}} & 0 \\
0 & 0 & 0 & 1 & 0 & 0 & 0 & 0 & -C_{\psi_4}S_{\theta_4}e^{i\phi_{54}} & 0 \\
0 & -S_{\psi_4}e^{-i\phi_{43}} & 0 & 0 & 1 & 0 & 0 & 0 & -iC_{\psi_4}C_{\theta_4}e^{i\phi_{54}} & 0 \\
0 & -C_{\psi_4}S_{\theta_4}e^{-i\phi_{43}} & 0 & 0 & 0 & 1 & 0 & 0 & 0 & 0 \\
0 & 0 & 0 & 0 & 0 & -C_{\psi_5}S_{\theta_5}e^{-i\phi_{54}} & 1 & 0 & 0 & 0 \\
0 & 0 & 0 & 0 & 0 & S_{\psi_5}e^{-i\phi_{54}} & 0 & 1 & 0 & 0 \\
0 & 0 & 0 & 0 & 0 & 0 & 0 & 0 & 1 & 0 \\
0 & 0 & 0 & 0 & 0 & -iC_{\psi_5}C_{\theta_5}e^{-i\phi_{54}} & 0 & 0 & 0 & 1
\end{bmatrix}. \tag{A.5}$$

Bibliography

[1]J. C. Maxwell, *A Treatise on Electricity and Magnetism* (Cambridge University Press, June 1873).

[2]E. H. Hall, "On a New Action of the Magnet on Electric Currents", American Journal of Mathematics **2**, 287 (1879).

[3]D. Morin, *Introduction to Classical Mechanics* (Cambridge University Press, June 2012).

[4]J. R. Hook and H. E. Hall, *Solid State Physics* (Wiley, 1995).

[5]S. H. Simon, *The Oxford Solid State Basics* (Oxford University Press, 2013).

[6]S. M. Girvin and K. Yang, *Modern Condensed Matter Physics* (Cambridge University Press, Feb. 2019).

[7]Y. Imry, *Introduction to Mesoscopic Physics* (Oxford University Press, 1997).

[8]K. v. Klitzing, G. Dorda, and M. Pepper, "New Method for High-Accuracy Determination of the Fine-Structure Constant Based on Quantized Hall Resistance", Physical Review Letters **45**, 494–497 (1980).

[9]B. Kramer, T. Ohtsuki, and S. Kettemann, *Random network models and quantum phase transitions in two dimensions*, Oct. 2005.

[10]R. E. Prange and S. M. Girvin, *The Quantum Hall Effect*, edited by R. E. Prange and S. M. Girvin, Graduate Texts in Contemporary Physics (Springer New York, New York, NY, 1990).

[11]K. von Klitzing, "The quantized Hall effect", Reviews of Modern Physics **58**, 519–531 (1986).

[12]A. C. M. de Oca and D. Martinez-Pedrera, "Role of impurities in stabilizing quantum Hall effect plateaus", Physical Review B **67**, 245310 (2003).

[13]J. E. Furneaux and T. L. Reinecke, "Novel features of quantum Hall plateaus for varying interface charge", Physical Review B **29**, 4792–4795 (1984).

[14]R. B. Laughlin, "Quantized Hall conductivity in two dimensions", Physical Review B **23**, 5632–5633 (1981).

[15]R. Shankar, *Principles of Quantum Mechanics* (Springer US, New York, NY, 1994).

[16]L. Landau, "Diamagnetismus der Metalle", Zeitschrift für Physik **64**, 629–637 (1930).

[17]K.-i. Nakamura, "Impurity Effect in Superconductors", Progress of Theoretical Physics **21**, 435–440 (1959).

[18]P. W. Anderson, "Absence of Diffusion in Certain Random Lattices", Physical Review **109**, 1492–1505 (1958).

[19]T. Brandes and S. Kettemann, eds., *Anderson Localization and Its Ramifications*, Vol. 630 (Springer Berlin Heidelberg, Berlin, Heidelberg, 2003).

[20]E. Noether, "Invariante Variationsprobleme", Nachrichten von der Gesellschaft der Wissenschaften zu Göttingen, Mathematisch-Physikalische Klasse **1918**, 235–257 (1918).

[21]J. Marion and S. Thornton, *Classical Dynamics of Particles and Systems* (Saunders College Publications, New York, 1995).

[22]M. E. Peskin, *An Introduction To Quantum Field Theory* (CRC Press, May 2018).

[23]C. N. Yang and R. L. Mills, "Conservation of Isotopic Spin and Isotopic Gauge Invariance", Physical Review **96**, 191–195 (1954).

[24]S. Blundell, *Magnetism in Condensed Matter* (Oxford University Press, 2001).

[25]C. N. Yang, M.-L. Ge, and Y.-H. He, *Topology and Physics* (World Scientific, Mar. 2019).

[26]D. J. Thouless, M. Kohmoto, M. P. Nightingale, and M. den Nijs, "Quantized Hall Conductance in a Two-Dimensional Periodic Potential", Physical Review Letters **49**, 405–408 (1982).

[27]M. Born and V. Fock, "Beweis des Adiabatensatzes", Zeitschrift fr Physik **51**, 165–180 (1928).

[28]D. J. Griffiths and D. F. Schroeter, *Introduction to Quantum Mechanics* (Cambridge University Press, Aug. 2018).

[29]M. V. Berry, "Quantal phase factors accompanying adiabatic changes", Proceedings of the Royal Society of London. A. Mathematical and Physical Sciences **392**, 45–57 (1984).

[30]M. P. do Carmo, *Differential Geometry of Curves and Surfaces* (Prentice-Hall, 1976).

[31]Bernevig B A and Hughes T L, *Topological Insulators and Topological Superconductors* (Princeton University Press, Apr. 2013).

[32]D. J. Griffiths, *Introduction to Electrodynamics* (Cambridge University Press, June 2017).

[33]S.-s. Chern, "Characteristic Classes of Hermitian Manifolds", The Annals of Mathematics **47**, 85 (1946).

[34]A. Hatcher, *Algebraic Topology* (Cambridge University Press, 2002).

[35]M. Nakahara, *Geometry, Topology and Physics* (Taylor & Francis Group, 2003).

[36]S.-s. Chern, *Complex Manifolds without Potential Theory* (Springer New York, New York, NY, 1979).

[37]S.-S. Chern, "A Simple Intrinsic Proof of the Gauss-Bonnet Formula for Closed Riemannian Manifolds", The Annals of Mathematics **45**, 747 (1944).

[38]R. Vein and P. Dale, *Determinants and Their Applications in Mathematical Physics*, Vol. 134 (Springer-Verlag, New York, 1999).

[39]M. Z. Hasan and C. L. Kane, "Topological insulators", Reviews of Modern Physics **82**, 3045–3067 (2010).

[40]P. Kotetes, *Topological Insulators* (Morgan & Claypool Publishers, Apr. 2019).

[41]B. A. Bernevig and S. C. Zhang, "Quantum spin hall effect", Physical Review Letters **96**, 10.1103/PhysRevLett.96.106802 (2006).

[42]B. A. Bernevig, T. L. Hughes, and S.-C. Zhang, "Quantum Spin Hall Effect and Topological Phase Transition in HgTe Quantum Wells", Science **314**, 1757–1761 (2006).

[43]M. König, S. Wiedmann, C. Brüne, A. Roth, H. Buhmann, L. W. Molenkamp, X.-L. Qi, and S.-C. Zhang, "Quantum Spin Hall Insulator State in HgTe Quantum Wells", Science **318**, 766–770 (2007).

[44]S.-Q. Shen, *Topological Insulators* (Springer, 2012).

[45]H. Tasaki, *Physics and Mathematics of Quantum Many-Body Systems* (Springer, 2020).

[46]D. C. Tsui, H. L. Stormer, and A. C. Gossard, "Two-Dimensional Magnetotransport in the Extreme Quantum Limit", Physical Review Letters **48**, 1559–1562 (1982).

[47]H. L. Stormer, D. C. Tsui, and A. C. Gossard, "The fractional quantum Hall effect", Reviews of Modern Physics **71**, https://doi.org/10.1103/RevModPhys.71.S298 (1999).

[48]R. Shankar, *Quantum Field Theory and Condensed Matter* (Cambridge University Press, 2017).

[49]N. Goldenfeld, *Lectures on Phase Transitions and the Renormalization Group* (CRC Press, 1992).

[50]L. Onsager, "Crystal Statistics. I. A Two-Dimensional Model with an Order-Disorder Transition", Physical Review **65** (1944).

[51]B. McCoy and T. T. Wu, *The Two-Dimensional Ising Model* (Harvard University Press, 1973).

[52]M. Kardar, *Statistical Physics of Fields* (Cambridge University Press, June 2007).

[53]J. Zinn-Justin, *Phase Transitions and Renormalization Group* (Oxford University Press, 2013).

[54]J. Cardy, *Scaling and Renormalization in Statistical Physics* (Cambridge University Press, Apr. 1996).

[55]F. D. M. Haldane, "Model for a Quantum Hall Effect without Landau Levels: Condensed-Matter Realization of the "Parity Anomaly"", Physical Review Letters **61**, 2015–2018 (1988).

[56]M. R. Zirnbauer, "Towards a theory of the integer quantum Hall transition: From the nonlinear sigma model to superspin chains", Annalen der Physik **506**, 513–577 (1994).

[57]A. Pruisken, "On localization in the theory of the quantized hall effect: A two-dimensional realization of the θ-vacuum", Nuclear Physics B **235**, 277–298 (1984).

[58]J. T. Chalker and P. D. Coddington, "Percolation, quantum tunnelling and the integer Hall effect", Journal of Physics C: Solid State Physics **21**, 2665–2679 (1988).

[59]D.-H. Lee, Z. Wang, and S. Kivelson, "Quantum percolation and plateau transitions in the quantum Hall effect", Physical Review Letters **70**, 4130–4133 (1993).

[60]D.-H. Lee, "Transitions between Hall plateaux and the dimerization transition of a Hubbard chain", Philosophical Magazine Letters **73**, 145–152 (1996).

[61]B. Huckestein and B. Kramer, "One-parameter scaling in the lowest Landau band: Precise determination of the critical behavior of the localization length", Physical Review Letters **64**, 1437–1440 (1990).

[62]W. Li, C. L. Vicente, J. S. Xia, W. Pan, D. C. Tsui, L. N. Pfeiffer, and K. W. West, "Scaling in plateau-to-plateau transition: A direct connection of quantum hall systems with the Anderson localization model", Physical Review Letters **102**, 10.1103/PhysRevLett.102.216801 (2009).

[63]K. Slevin and T. Ohtsuki, "Critical exponent for the quantum Hall transition", Physical Review B - Condensed Matter and Materials Physics **80**, 10.1103/PhysRevB.80.041304 (2009).

[64]M. R. Zirnbauer, "Marginal CFT perturbations at the integer quantum Hall transition", Annals of Physics **431**, 168559 (2021).

[65]P. M. Chaikin and T. C. Lubensky, *Principles of Condensed Matter Physics* (Cambridge University Press, June 1995).

[66]M. E. Fisher, "The renormalization group in the theory of critical behavior", Reviews of Modern Physics **46**, 597–616 (1974).

[67]H. D. Politzer, "Reliable Perturbative Results for Strong Interactions?", Physical Review Letters **30**, 1346–1349 (1973).

[68]S. Coleman and E. Weinberg, "Radiative Corrections as the Origin of Spontaneous Symmetry Breaking", Physical Review D **7**, 1888–1910 (1973).

[69]K. G. Wilson, "Renormalization Group and Critical Phenomena. I. Renormalization Group and the Kadanoff Scaling Picture", Physical Review B **4**, 3174–3183 (1971).

[70]M. R. Zirnbauer, "Toward a theory of the integer quantum Hall transition: Continuum limit of the Chalker-Coddington model", Journal of Mathematical Physics **38**, 2007–2036 (1997).

[71]L. P. Kadanoff, "Scaling laws for ising models near Tc", Physics Physique Fizika **2**, 263–272 (1966).

[72]H. A. Fertig and B. I. Halperin, "Transmission coefficient of an electron through a saddle-point potential in a magnetic field", Physical Review B **36**, 7969–7976 (1987).

[73]D. P. Arovas, M. Janssen, and B. Shapiro, "Real-space renormalization of the Chalker-Coddington model", Physical Review B **56**, 4751–4759 (1997).

[74]P. Cain, M. E. Raikh, and R. A. Römer, "Real-Space Renormalization Group Approach to the Quantum Hall Transition", Journal of the Physical Society of Japan **72**, 135–136 (2003).

[75]P. Cain, R. A. Römer, M. E. Raikh, and R. A. Römer, "Renormalization group approach to the energy level statistics at the integer quantum Hall transition", Physica E: Low-dimensional Systems and Nanostructures **18**, 126–127 (2003).

[76]I. A. Gruzberg, A. Klümper, W. Nuding, and A. Sedrakyan, "Geometrically disordered network models, quenched quantum gravity, and critical behavior at quantum Hall plateau transitions", Physical Review B **95**, 125414 (2017).

[77]A. Klümper, W. Nuding, and A. Sedrakyan, "Random network models with variable disorder of geometry", Physical Review B **100**, 140201 (2019).

[78]I. Mukherjee and P. K. Mohanty, "A unified picture of continuous variation of critical exponents", (2023).

[79]N. Khan, P. Sarkar, A. Midya, P. Mandal, and P. K. Mohanty, "Continuously varying critical exponents beyond weak universality", Scientific Reports **7**, 10.1038/srep45004 (2017).

[80]J. Chahine, J. R. D. d. Felicio, and N. Caticha, "Non-universal exponents and marginal operators via a Monte Carlo renormalisation group", Journal of Physics A: Mathematical and General **22**, 1639–1645 (1989).

[81]A. Taroni, S. T. Bramwell, and P. C. Holdsworth, "Universal window for two-dimensional critical exponents", Journal of Physics Condensed Matter **20**, 10.1088/0953-8984/20/27/275233 (2008).

[82]F. C. Alcaraz and M. N. Barber, "On the critical behavior of the Ising model with mixed two- and three-spin interactions", Journal of Statistical Physics **46**, 435–453 (1987).

[83]R. F. Andrade and H. J. Herrmann, "Percolation model with continuously varying exponents", Physical Review E - Statistical, Nonlinear, and Soft Matter Physics **88**, 10.1103/PhysRevE.88.042122 (2013).

[84]K. Shida, R. Sahara, M. N. Tripathi, H. Mizuseki, and Y. Kawazoe, "Conductivity percolation on a square lattice with core-shell particles", Materials Transactions **51**, 771–774 (2010).

[85]S. Roux, E. Guyon, and D. Sornette, "Hull percolation", Journal of Physics A: Mathematical and General **21**, L475–L482 (1988).

[86]S. Ryu, C. Mudry, H. Obuse, and A. Furusaki, "The 2 network model for the quantum spin Hall effect: Two-dimensional Dirac fermions, topological quantum numbers and corner multifractality", New Journal of Physics **12**, 10.1088/1367-2630/12/6/065005 (2010).

[87]K. Kobayashi, T. Ohtsuki, and K. Slevin, "Critical Exponent for the Quantum Spin Hall Transition in 2 Network Model", in Localisation 2011 (Dec. 2012), pp. 114–119.

[88]J. H. Son and S. Raghu, "Three-dimensional network model for strong topological insulator transitions", Physical Review B **104**, 125142 (2021).

Index